# Wireless MEMS drug delivery device enabled by a micromachined Nitinol actuator as a pumping mechanism

by

Jeffrey Chun Kit Fong

B.Sc. Engineering Physics, University of Alberta, 2012

A thesis submitted in partial fulfillment of

the requirements for the degree of

Master of Applied Science

in

The Faculty of Graduate and Postdoctoral Studies

(Electrical & Computer Engineering)

The University of British Columbia

(Vancouver)

December 2014

## Abstract

Traditional drug delivery methods utilize systemic administration where the medication is circulated through the entire body. These methods require a high dosage at the point of entry in order to reach the therapeutic level at the targeted location and can result in serious side effects. Implantable drug delivery devices can be used to increase efficacy by targeting specific regions in the body and by safely using higher drug concentrations. Microfabrication allows for the creation of these minimally invasive devices to treat conditions not previously possible due to the limited amount of space surrounding the target area. Devices with passive releasing mechanisms have been commercialized but ones with active mechanisms are still in the works.

In this thesis, a shape memory alloy (SMA) actuator is micromachined into a rectangular, planar coil to perform cantilever-like actuation. The SMA-coil actuator forms a passive resonant circuit that functions as a wireless heat source activated using external radio-frequency (RF) electromagnetic fields. $SiO_2$ stress layers are selectively patterned on the Nitinol SMA structure to manipulate the cantilever profile at the nominal cold state. RF radiation with varying field frequencies showed strong frequency dependence of wireless heating, actuation displacement, and force generation by several actuators with resonant frequencies of 170-245 MHz. When excited at resonance, these actuators exhibited maximum out-of-plane displacement and force of 215 μm and 71 mN, respectively. The actuator was integrated into a 10.0×10.5×2.1 $mm^3$ polyimide-packaged chip containing a micromachined Parylene-C pump chamber to force the release of the drug from the reservoir by wirelessly activating the actuator. Experimental operation of the prototypes showed successful release of the test agents from devices placed in liquid and excited by radiating tuned RF fields with an output power of 1.1 W. These tests revealed a single release volume of 219 nL, suggesting that the device's capacity of 76 μL is equivalent to ~350 individual ejections. Thermal behavior of the activated device is also reported in detail. This proof-of-concept prototype validates the effectiveness of wireless RF pumping for fully controlled, long-lasting drug delivery, a key step towards enabling patient-tailored, targeted local drug delivery through highly miniaturized implants.

## Preface

Parts of this thesis have been published in [1] where the design, fabrication, and testing of the entire drug delivery device are discussed. Other parts of this thesis have been submitted as [2] where detailed aspects of the Nitinol actuator are discussed. In those publications, the work of the co-authors Dr. Kenichi Takahata, my research supervisor, and Zhiming Xiao, a postdoctoral fellow who helped with Nitinol micromachining, is acknowledged; however, I conducted all of the design and testing, and most of the fabrication.

[1] J. Fong, Z. Xiao, and K. Takahata, "Wireless implantable chip with integrated nitinol-based pump for radio-controlled local drug delivery," *Lab on a Chip*, DOI: 10.1039/C4LC01290A, 2015.

[2] J. Fong, Z. Xiao, and K. Takahata, "Micromachined Rectangular-Spiral-Coil Actuator for Radio-Controlled Cantilever-Like Actuation," submitted to a peer-reviewed journal.

## Table of Contents

## List of Figures

## List of Abbreviations

| | |
|---|---|
| **DDD** | Drug Delivery Device |
| **EC** | Electrical Conductivity |
| **IPA** | Isopropyl Alcohol |
| ***LC*** | Inductor-Capacitor |
| **PECVD** | Plasma Enhanced Chemical Vapor Deposition |
| **μEDM** | Micro-Electro-Discharge Machining |
| **MEMS** | Micro-Electro-Mechanical Systems |
| **RF** | Radio Frequency |
| **SMA** | Shape Memory Alloy |

## Acknowledgements

I would like to thank my supervisor Kenichi Takahata for his patience, guidance, and motivation throughout my studies at the University of British Columbia. I definitely could not have completed all this research without his input.

I would like to acknowledge CMC Microsystems for the provision of products and services that facilitated this research, including COMSOL Multiphysics, Tanner EDA L-Edit, and MNT Financial Assistance. I would like to thank the Natural Sciences and Engineering Research Council of Canada (NSERC) for providing me with financial assistance through a Canada Graduate Scholarship (CGS-M).

I would also like to thank Daniel Brox for cleanroom equipment training; Zhiming Xiao for SEM imaging and μEDM processing and training; and Xing Chen, Masoud Dahmardeh, and Babak Assadsangabi for their valuable advice.

Finally and most importantly, I would like to thank my parents and my girlfriend for allowing me this opportunity to pursue my Master's degree away from home and supporting me throughout the entire process.

**Dedication**

*To Felicia and my parents*

# Chapter 1: Introduction

## 1.1 Background and Motivation

Traditionally, the most common methods of drug delivery include oral, topical, inhalation, and injection. Besides topical application where the effect is generally localized, these methods typically utilize systemic administration, meaning that the medication is delivered through the circulatory system and affects the whole body. In systemic delivery, high dosages are required at the point of entry in order for the desired therapeutic level to be reached at the targeted location. This undesirable situation is necessary not only because the drug is diluted throughout the body but also because of the first pass effect for oral delivery [1] and the diffusion barriers of certain tissue [2]. The first pass effect is caused by drug metabolism where the drug's chemical compounds are converted into hydrophilic products which are more readily excreted. As a result, oral drug concentration is significantly reduced before it even enters the circulatory system. Regarding diffusion barriers, abscesses are collections of infectious material which are "walled-off" from circulation, so high doses of antibiotics are required to pierce the abscess wall; but in some scenarios the drug cannot enter the abscess at all [2]. Another example is the eye's blood-retina barrier which only allows oxygen and nutrients to pass, blocking larger molecules from the circulatory system [3]. In this case, it is not even possible to treat diseases of the eye with systemic administration. And although drugs can be tailored to target specific organs or cells, serious systemic side effects may still occur, damaging otherwise healthy tissue. For example, chemotherapy targets rapidly dividing cells like cancer cells but also targets the cells in bone marrow and hair follicles, resulting in immunosuppression and hair loss, respectively [4], [5]. Localizing drug delivery to prevent the previously mentioned problems could be performed using implantable devices. Passive devices rely on diffusion to continuously release the drug at a controlled rate and can be made using either a diffusion barrier to encase a drug reservoir or a polymer matrix to soak up the drug. Gliadel wafers, Zoladex implants, and Retisert are commercially available devices to treat gliobastoma, prostate cancer, and chronic non-infectious uveitis, respectively [6]–[8]. These devices can produce better control over drug concentration compared to bolus administration because bolus administration results in

overshooting the drug concentration and less time within the therapeutic range. However, this constant release profile might not be ideal for treating such issues; active devices may be more useful as the dosage can be varied and also be tuned to individual patients.

An active device with dimensions in the centimeter range containing the drug delivering mechanism, batteries for powering, and complex circuitry for operation management may be highly invasive and pose biocompatibility issues as an implant. Advances in microfabrication have resulted in significant interest towards building drug delivery devices (DDD) with micro-electro-mechanical systems (MEMS) technology [9]–[12]. These active devices with small form factors up to the millimeter range could be implanted directly at the targeted site with minimally invasive surgery. Some devices have been developed to selectively release individual drug filled reservoirs from an array of micro-reservoirs using an electrothermal [13]–[15] or electrochemical [16]–[18] mechanism. Each reservoir is sealed with a metal membrane and can be opened by applying electrical power. The electrothermal mechanism is being pursued by the company MicroCHIPS for several different applications including contraception, osteoporosis, and multiple sclerosis [19]. Its osteoporosis application was the first wirelessly controlled MEMS-based DDD to be tested in humans [20]. Other DDDs currently being researched utilize a variety of mechanical and non-mechanical micropumps [21]. Mechanical micropumps have moving parts such as pumping diaphragms and check valves; and although non-mechanical micropumps with no moving parts, which are less prone to failure, could potentially extend the device's lifetime, they have not been widely used because their pumping ability highly depends on the properties of the fluid being moved [11].

Mechanical micropumps typically use a positive displacement pump with a flexible diaphragm, an inlet valve, and an outlet valve as shown in Figure 1.1. Oscillatory movement of the diaphragm creates under pressure where fluid is drawn into the pumping chamber and over pressure where fluid is forced out. The valves are very important as they ensure fluid flow in the proper direction. Valves can either be passive [22], [23] or active [24], [25]; passive valves require a difference in pressure across them to open or close, whereas active valves can be controlled independent of the pressure but require more complicated fabrication.

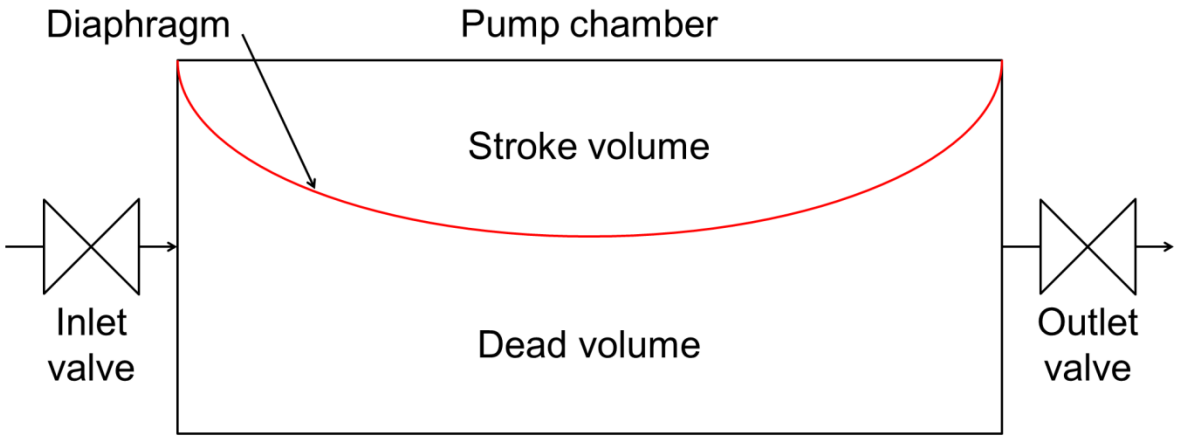


Figure 1.1: A basic diaphragm-type pump

Active, reservoir-based MEMS DDDs offer the greatest potential in many applications because they have higher drug loading compared to infused polymer matrix devices, they are refillable, and the dosages can be tuned for individual patients. They could be used to treat a wide range of conditions including brain tumors, chronic pain syndromes, infectious abscesses, chronic eye diseases, and diabetes [2], [20], [26]. Benefits over traditional forms of drug delivery comprise of reducing the number of surgeries required, using higher drug concentrations at localized regions for greater efficacy, reducing the side effects, and not having to rely on patients to stay on top of their medication.

Microactuators are used to perform work on the diaphragm of mechanical micropumps and have been enabled with a variety of mechanisms, including electrostatic [27], piezoelectric [28], electromagnetic [29], electrothermal [30], electrochemical [31], and shape memory alloy (SMA) [32]. As every mechanism has its advantages and disadvantages [21], [33], choosing the appropriate mechanism depends on the intended application. In general, electrostatic actuators have low power consumption and fast response times, but require high voltages and only produce small displacements. Piezoelectric actuators generate large forces and have fast response times but also require high voltages for small displacements. Electromagnetic actuators generate large forces but do not benefit from miniaturization and often require non-standard techniques for micromachining of magnetic materials. Electrothermal actuators also generate large forces but consume a large amount of power to produce relatively small displacements. Implementing these mechanisms usually requires

connecting the microdevices to an external power source via electrical wires; but this is not feasible for many applications such as wireless sensor/actuator networks, microrobotics, and medical implants. Batteries could be included for such applications; however, they have a limited lifetime and would increase the overall device size, limiting their application range especially in the medical areas. Passive, wireless actuation does not require an internal power supply or active circuitry for actuation control and may be more useful for the aforementioned applications. Wirelessly powered actuators have been reported using a few different mechanisms, including electrostatic actuation via surface acoustic waves [34] and magnetic fields [35], magnetic actuation [36], [37], heating via energy beams for bimetallic actuation [38], and SMA actuation [39], [40].

### 1.2 Thesis Objectives

The aim of this thesis is to design, fabricate, and test a wirelessly powered, minimally invasive DDD with overall dimensions of about 10×10×2 $mm^3$. The device will utilize a diaphragm-type pump with micro check valves to direct the drug flow from a reservoir into the pumping chamber and then out of the device. These components will be made entirely of biocompatible materials polyimide and Parylene-C. And by making use of the research group's expertise with Nitinol, a SMA actuator will be created and used to activate the DDD.

### 1.3 Thesis Outline

Chapter 2 reviews existing efforts in creating MEMS DDDs with different pumping mechanisms. Then it focuses on technologies to be utilized in the fabricated device including Nitinol, wireless resonant heating, and micro check valves. Chapter 3 goes through the designs of the individual components so that they can be combined to form a miniscule device. Chapter 4 details the fabrication steps of all the components which include the usage of photolithography, wet and dry etching, thin film deposition, electroplating, and micro-electro-discharge machining (μEDM). Chapter 5 describes the experimental set-ups and presents the collected data. The actuator is tested for resonance, wireless heating, actuation displacement, and actuation force while the pump chamber is tested for pumping volume. Then the two components are combined and tested together. Chapter 6 summarizes the work that has been done in this thesis and provides possibilities of improving the device's design.

## Chapter 2: Related Work

A DDD was fabricated that could be manually pumped by pressing the device with one's finger [26]. It consisted of a polydimethylsiloxane (PDMS) reservoir and a cannula with an integrated check valve. Its purpose was to treat ocular diseases while reducing the number of invasive surgeries, thus reducing the chance to cause trauma to the eye. Only one surgery is required to insert the cannula into the eye through a small incision. The reservoir is located several millimeters away and can be refilled with a needle. Then the device was improved by incorporating an electrochemical pump rather than having to manually pump it [41], [42]. Within the reservoir was a Parylene chamber containing water and a pair of interdigitated electrodes. When electrical current was passed through the electrodes, water molecules would be split into hydrogen and oxygen gas; because the gases occupy a larger volume, the chamber expands and forces the drug out the catheter as shown in Figure 2.1. In the latest revision of this device, an inductor-capacitor (*LC*) tank, a rectifying circuit, and a voltage regulator were incorporated to allow for wireless activation [31].

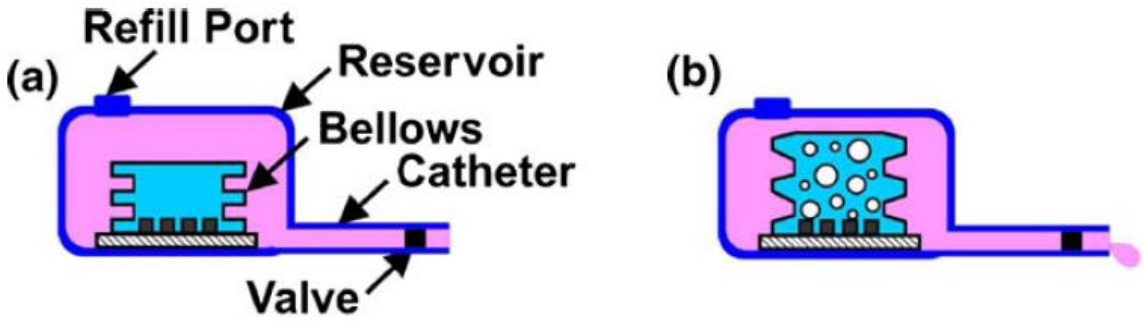


Figure 2.1: (a) Components of the electrochemical DDD and (b) its working principle [42] (© 2012 Springer New York LLC, by permission)

Another implantable device was fabricated that did not incorporate any pumping mechanism but could still be wirelessly controlled with active microvalves [43]. Basically, it was a reservoir with release holes that could be opened and closed using a thermoresponsive hydrogel. A radio frequency (RF) magnetic field would heat the planar *LC* circuit beneath the hydrogel microvalves and cause them to shrink in size, allowing the drug to diffuse out as shown in Figure 2.2.

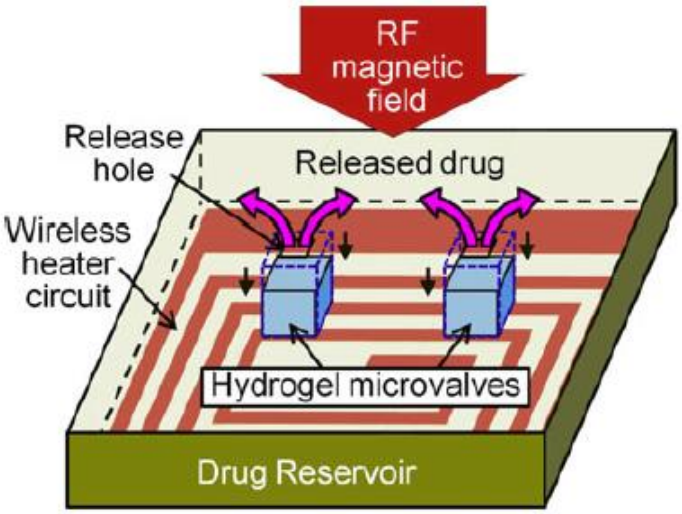


Figure 2.2: Wirelessly activated hydrogel microvalves [43] (© 2010 Springer New York LLC, by permission)

When the frequency of the magnetic field matches the resonant frequency of the *LC* circuit ($f_R = \left(2\pi\sqrt{LC}\right)^{-1}$, where $L$ and $C$ are the inductance and capacitance of the circuit, respectively), the reactance of the inductor and the capacitor cancel out and the power consumed by the circuit can be simply expressed as

$$P = v^2/R \tag{2.1}$$

where $R$ is the resistance of the circuit and $v$ is the inductively induced voltage. This results in maximum power consumption and conversion into thermal energy. Resonant inductive heating is beneficial over non-resonant inductive heating as the field strength required for a desired level of heating is much lower, thus exposing the human body to less electromagnetic radiation. In addition, the frequency selectivity of heating potentially allows more precise and safer device operation. Both of the presented devices were controlled wirelessly but the hydrogel device relied on diffusion to release the drug whereas the other device used an electrochemical micropump with variable flow rate. The benefit of the hydrogel device though is that it used a simple *LC* circuit for wireless control; there was no need for a rectifying circuit or a voltage regulator. These extra components increase the overall device size and complexity, potentially with more possibilities for failure.

This next device was not meant for implantation but does relate to drug delivery. A microsyringe was fabricated using a Parylene reservoir and three Nitinol SMA actuators for pumping [44]. The shape memory effect of Nitinol allows it to be deformed at a low temperature and then return to its original, pre-deformed shape once it is heated past its transition temperature. SMA actuators offer attractive features of large forces and high work output per unit volume without the need for high voltages. In particular, Nitinol is used in many applications because it is also biocompatible, ductile, and resistant to corrosion [45]–[48]. Although SMA actuation is relatively slow as it relies on metallurgical phase transition, this drawback is not a major concern in many cases, leading to studies for a broad range of applications including biomedical devices [49]–[53] and robotics [54]–[56]. Nitinol has two different phases, austenite and martensite; transformation between the phases depends on its temperature as shown in Figure 2.3. $A_s$ and $A_f$ (or $T_a$) are the temperatures where the transition from martensite to austenite starts and finishes. Similarly, $M_s$ and $M_f$ are the temperatures where the transition from austenite to martensite starts and finishes.

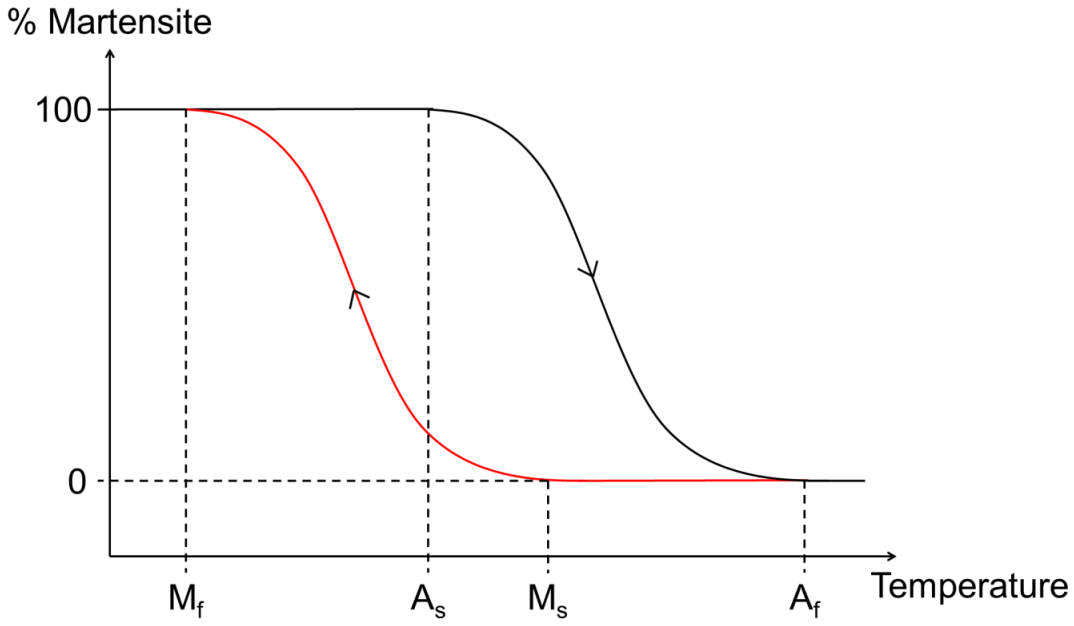


Figure 2.3: Typical hysteresis loop of Nitinol

Just like the previous device, *LC* circuits were used as wireless resonant heaters for activation. Three separate, planar *LC* circuits were fabricated next to one another with slightly different capacitances to target different resonant frequencies as shown in Figure 2.4.

Nitinol cantilever actuators were bonded directly to them to receive the thermal energy. By having three wireless heaters at different resonant frequencies, each heater and corresponding actuator could be controlled independently by modulating the frequency of the RF field.

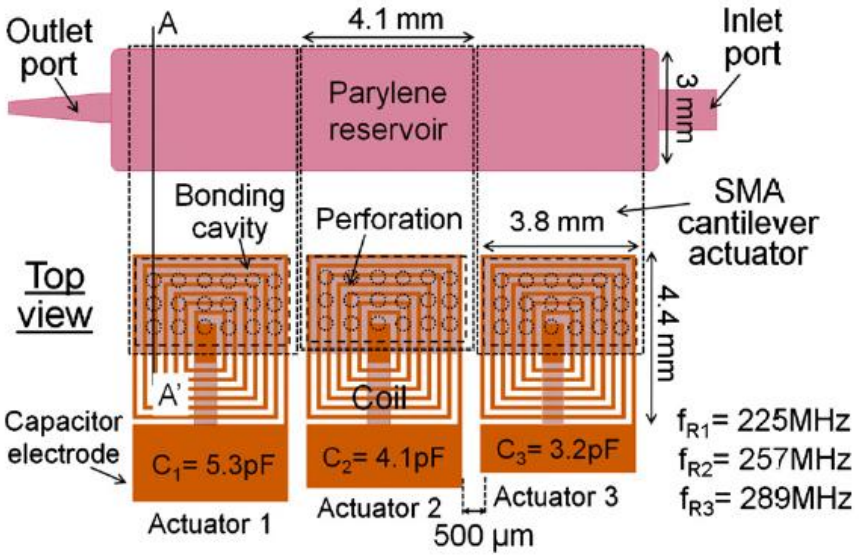


Figure 2.4: Design of the microsyringe using wireless heaters and Nitinol actuators [44]


The free end of the cantilever actuators had to be deformed in order for the Parylene reservoir to be placed underneath and so the actuators could return to their original (flat) shape to compress the reservoir during heating. To do so, a layer of silicon dioxide was deposited on the bottom side of the Nitinol at a temperature (390 °C) higher than $A_f$. $SiO_2$ was used as a stress layer to exploit two mechanisms that work together: 1) Plasma-enhanced chemical vapor deposition (PECVD) of $SiO_2$ results in intrinsic compressive stress which depends on the processing conditions [57]; 2) $SiO_2$ has a smaller coefficient of thermal expansion ($0.5\times10^{-6}$ /°C [58]) than that of Nitinol ($6.6\text{-}11\times10^{-6}$ /°C depending on the phase [59]). These two mechanisms combine so that PECVD $SiO_2$ deposited at elevated temperatures leads to compressive stress after cooling it down, bending the bilayer away from the side with the oxide when the Nitinol is in its cold (martensitic) state. It may have been possible to use this device in a peristaltic fashion as a continuous pump, but instead the reservoir was filled from the inlet port and then sealed off. To eject the fluid, actuator 3 in Figure 2.4 is activated to compress a third of the reservoir, then actuator 2 is also activated to

compress another third. Finally, all the actuators are activated together to completely compress the reservoir. To activate N heaters, the field frequency is modulated between the different resonant frequencies; so each frequency only gets $1/N^{th}$ of the total time the magnetic field is on for. To compensate for the temperature drop when the field frequency was not targeting a particular heater, the RF power had to be increased.

An aspect of the microsyringe to be improved upon is heating of the actuator. Even with good thermal contact between the heater and the actuator, there will be some delay in heating between them. Also, less than half of the actuator was actually in contact with the heater. The heat had to transfer from the planar coil to the bonded region of Nitinol and then distribute along the length of the cantilever. As noted in the paper, the difference in temperature between the ends of the actuator reached close to 40 °C during actuation. A new Nitinol actuator was produced to improve the temporal response and was reported to be 2-3× faster than the previous actuator [60]. In this design, the heating circuit and actuator were combined into a single unit; Nitinol was machined into a planar coil structure to act as an inductor. By depositing a $SiO_2$ layer on strategic areas of the coil as shown in Figure 2.5, out-of-plane displacement was achieved with the center of the coil at the maximum displacement as shown in Figure 2.6.

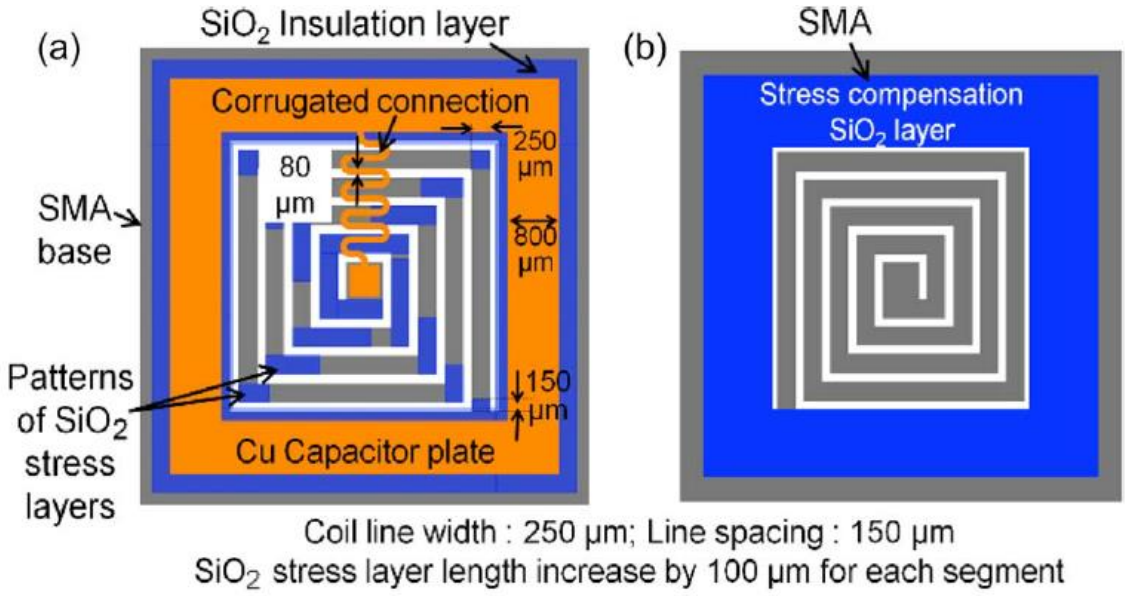


Figure 2.5: (a) Back side and (b) front side of the Nitinol coil actuator with strategic placement of the $SiO_2$ stress layer [60] (© 2013 IEEE, by permission)

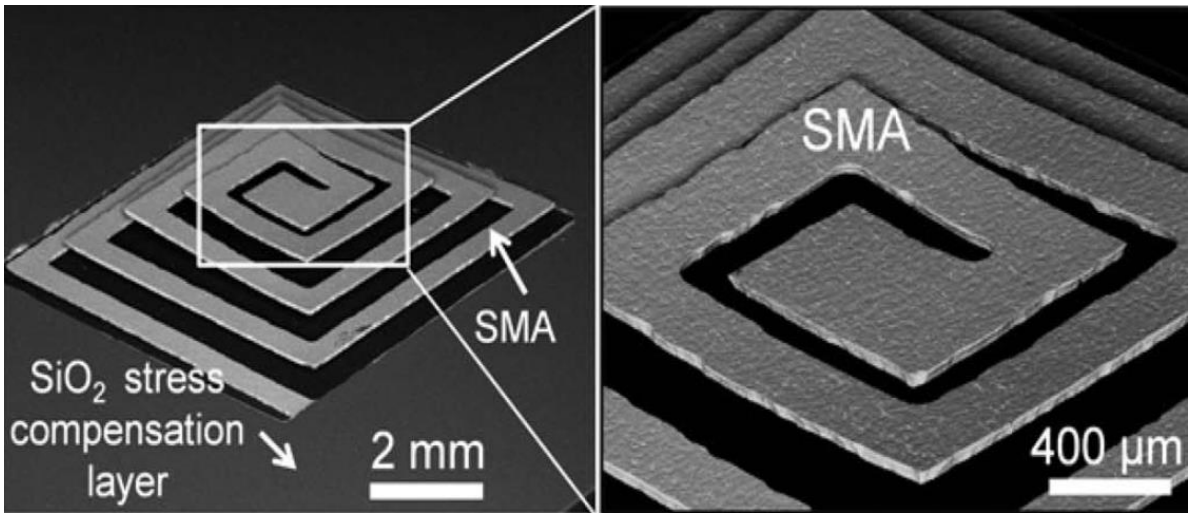


Figure 2.6: Out-of-plane displacement of the spiral coil actuator in martensite phase [60] (© 2013 IEEE, by permission)

The Nitinol surrounding the coil is used as one of the parallel plate capacitor electrodes; and $SiO_2$ and SU-8 are used as the dielectric layer. Electroplated copper is used as the other capacitor electrode and to make a corrugated connection between the capacitor and the center of the coil, completing the *LC* circuit. This device exhibited faster response because rather than transferring heat from a separate component, Joule heating was occurring directly in the Nitinol.

Check valves are critical to the success of a positive displacement pump. They should open for forward fluid flow and close for reverse flow. Many different types of micro check valves have been investigated, some that work in-plane [61]–[63] and others that work out-of-plane [64], [65]. An in-plane, piston-type microvalve was made inside a microfluidic channel as shown in Figure 2.7 [61]; the non-stick polymer piston is able to move freely along the constrained channel. During forward flow, the piston is pressed against the right stop but the fluid is allowed to flow through the top bypass channel. During reverse flow, the piston is seated against the left stop, blocking all fluid flow. Other in-plane check valves were designed to mimic the valves found in the cardiovascular system of humans which have simple structures and soft tissues [62], [63]. 4-hydroxylbutyl acrylate (4-HBA) is the elastic material used to make the check valves for the micropump shown in Figure 2.8.

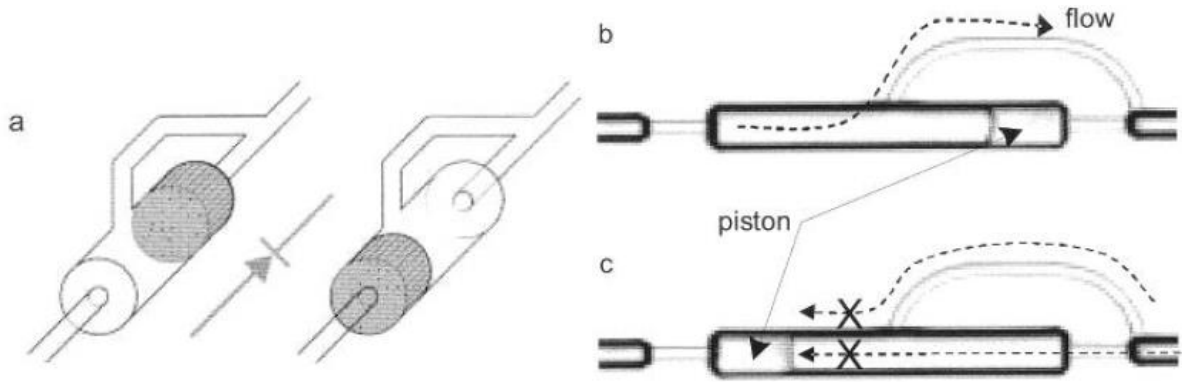


Figure 2.7: (a) In-plane, piston-type check valve during (b) forward fluid flow and (c) reverse fluid flow (Reprinted (adapted) with permission from [61]. © 2002 American Chemical Society.)

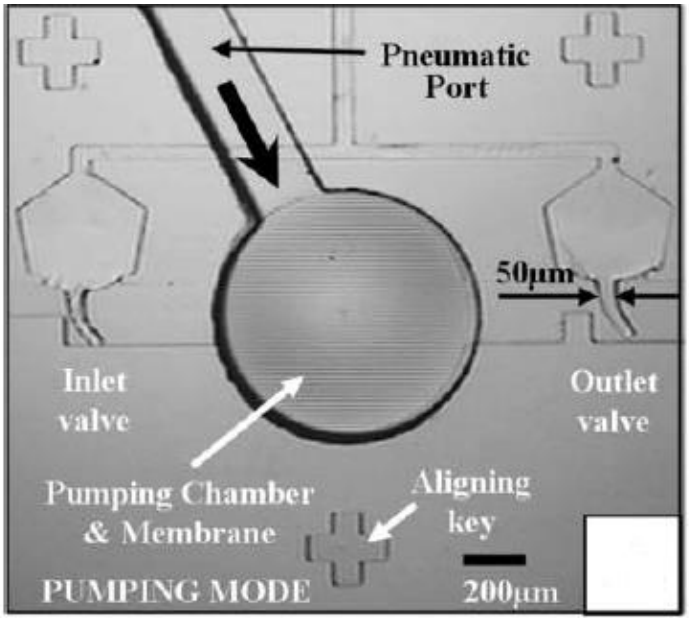


Figure 2.8: Pneumatic micropump utilizing 4-HBA in-plane check valves [62] (© 2006 The Royal Society of Chemistry, by permission)

An out-of-plane check valve was fabricated using Parylene as the valve disc and silicon as the valve seat as shown in Figure 2.9 [64]. Four S-shaped beams were used to tether the valve disc, making it twist upwards during forward flow. The length and low stiffness of the tethers resulted in large vertical displacement of the disc and minimal flow resistance. Other out-of-plane valves were designed to reduce the flow resistance further by completely eliminating the tethers [23]. The floating disc design uses a valve cap to keep the disc within

a confined region as shown in Figure 2.10. By changing the structure of the valve cap and seat, two very different valves are produced. The first design (Figure 2.10(a)) works as a typical check valve where any forward fluid flow is allowed and reverse flow is blocked. The second design (Figure 2.10(b)) still blocks reverse flow but only allows forward flow within a certain pressure range. This works because of a two-level valve seat; below the threshold pressure, the disc sits on the valve seat's top level and completely blocks the fluid path. But above the threshold pressure, the disc deforms and the trenches in the top seat level allows for fluid flow. And then if the forward pressure gets too high, the disc becomes highly bent and completely seals off the bottom seat level. Such a valve could be useful in implantable DDDs to prevent accidental release of the drug during abnormal pressure spikes; for example, a patient with an ocular device rubbing his or her eyes.

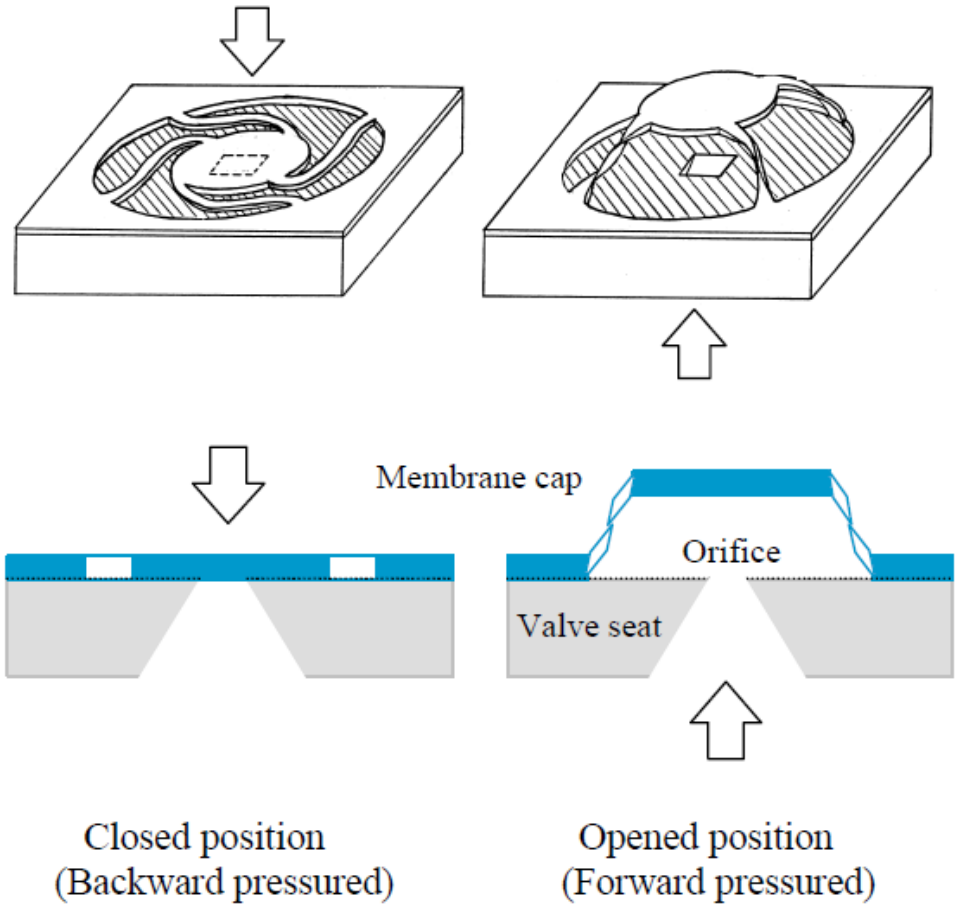


Figure 2.9: Out-of-plane Parylene microvalve with long S-shaped tethers [64] (© 1999 IEEE, by permission)

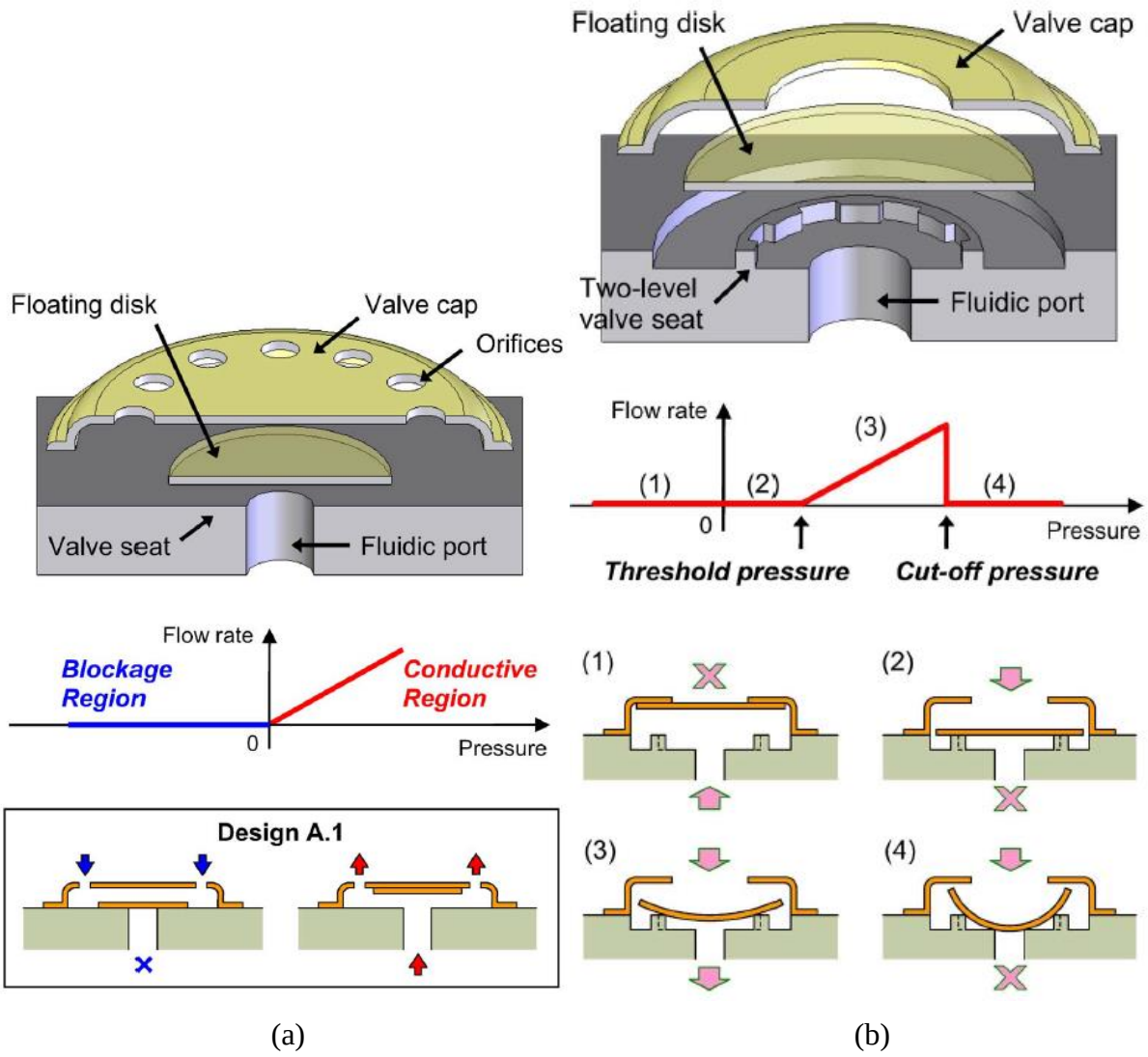


Figure 2.10: Floating disc, Parylene microvalves with (a) regular check valve behavior and (b) pressure-bandpass behavior [23] (© 2008 IEEE, by permission)

In this thesis, a MEMS DDD will be developed partly with ideas from the previously mentioned works. The pumping chamber will contain out-of-plane check valves similar to the one in Figure 2.9 rather than the more complex ones in Figure 2.10 to simplify the fabrication process. A Nitinol actuator will be chosen for pumping of the device because of the research group's expertise with this SMA. To implement wireless actuation, an *LC* circuit will be used for inductive resonant heating of the Nitinol. And to ensure fast response of the actuator, the actuator and the *LC* heater will be made into a single component, similar to the

design shown in Figure 2.5. However, one weakness of this self-heating design is that it only produces a maximum force of 30 mN [60] which is very small when compared to the similarly sized cantilever design, with a separate wireless heater, in Figure 2.4 with 840 mN [44]. Another weakness is that the design does not allow for easy coupling between actuation and the element being moved since the actuation location is at the center of the coil. The aim of this study is to combine the benefits of both actuators: faster response, larger actuation force, and easier integration with a more commonly used form factor.

# Chapter 3: Device Design

## 3.1 Actuator

Towards addressing the issues of the previously developed Nitinol wireless actuators noted in Chapter 2, a micromachined Nitinol actuator was designed, as shown in Figure 3.1, to offer cantilever-like motion with increased maximum force for the drug delivery application. The micromachined coil structure allows for wireless heating directly in the Nitinol via resonant RF fields. With it being rectangular-shaped, the longitudinal coil lines act as cantilever structures to produce out-of-plane displacements during heating. Cantilevers are one of the most common MEMS actuators; therefore, this new design could significantly expand the applicability of wireless MEMS actuators in biomedical, robotics, and other fields beyond this particular DDD application.

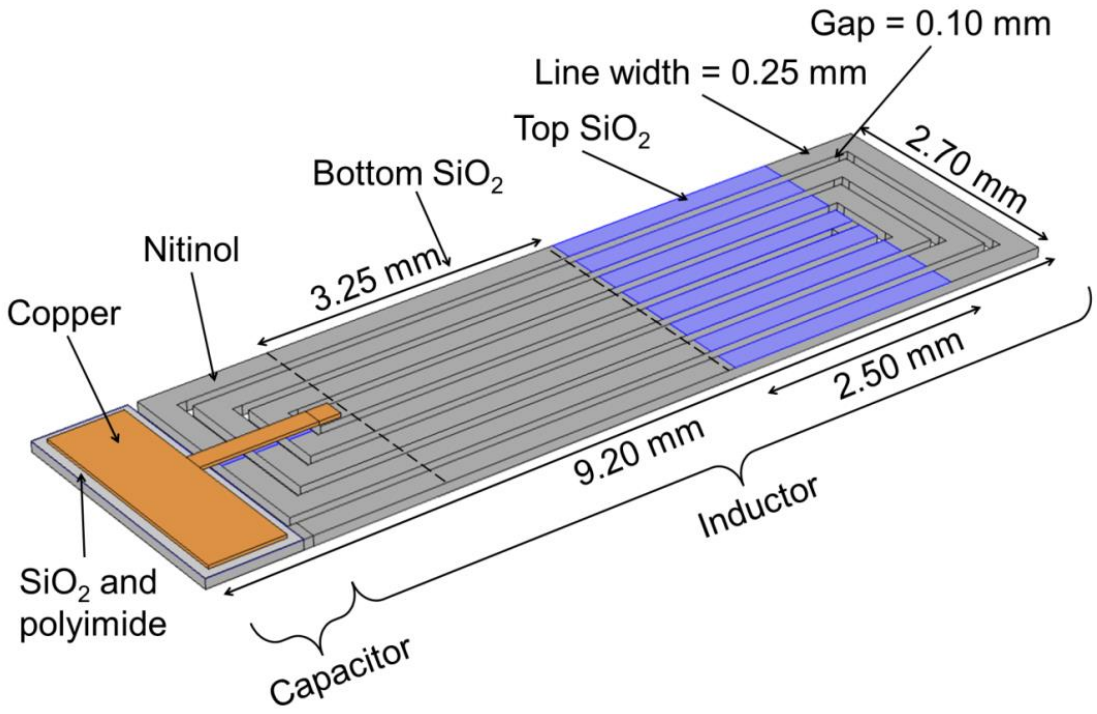


Figure 3.1: Design of the rectangular-coil actuator for cantilever-like actuation

The large rectangular area on the left side is used as part of the capacitor and is the fixed end of the cantilever. The total length of the actuator was set to less than 10 mm (9.2 mm) so it could fit within a ~10×10 $mm^2$ device. The bottom oxide is used to bend the free end

upwards while the top oxide is used to counteract the slope caused by the bottom oxide. The aim of the latter oxide is to keep the tip portion of the cantilever parallel with the substrate plane; this is practical in many cases that require forces applied to an object on the substrate to be along the vertical direction (not the case with an angled cantilever tip). The length and thickness of the oxide layers were adjusted so the free end would be relatively flat and allow for a box-like pump chamber to fit neatly underneath without any major gaps. These dimensions were determined through finite-element analysis (FEA) performed using COMSOL Multiphysics® 4.3b. The Nitinol thickness was chosen to be 100 μm. Thicker Nitinol generates a larger actuation force; however, this is a tradeoff for the amount of displacement with a given stress (oxide) layer thickness. By using an oxide deposition temperature of 290 °C and defining the physical properties of Nitinol [59], [66], 2-μm-thick $SiO_2$ on both sides of the Nitinol produced the simulation shown in Figure 3.2 with a relatively flat free end and a maximum displacement of 230 μm when the Nitinol is in its cold phase.

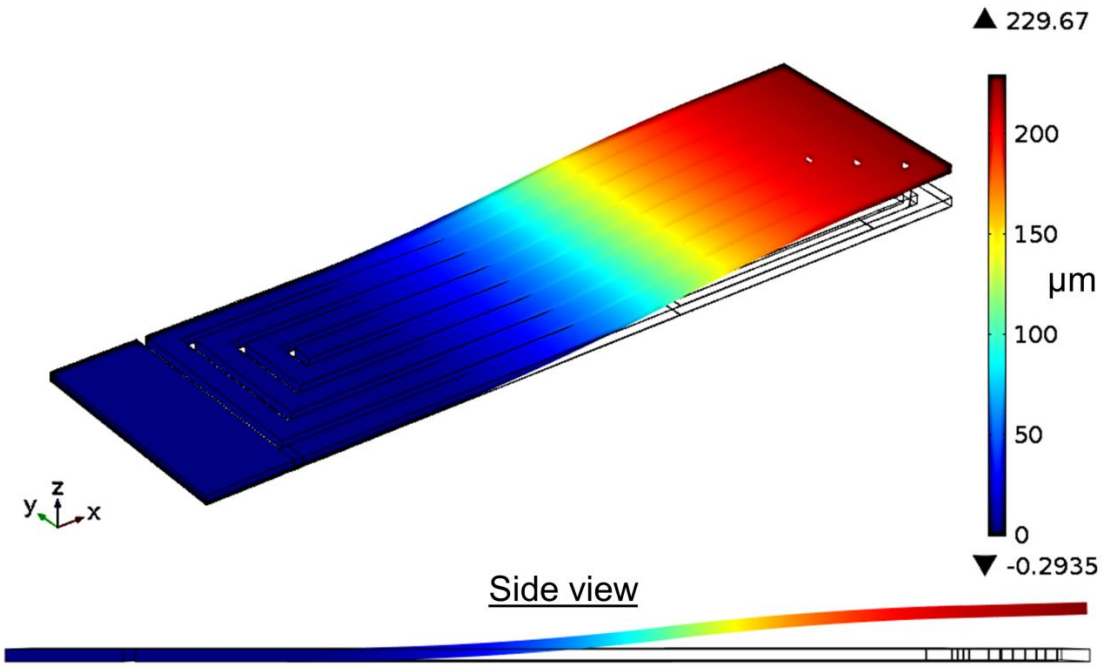


Figure 3.2: FEA simulation showing the free end on the right side with an out-of-plane displacement of 230 μm at room temperature; side view of the displaced actuator (bottom) shows a relatively flat profile around its free end

The next task was to design the inductance and capacitance of the actuator for a resonant frequency in the megahertz range. The coil's turn width was chosen to be 250 μm with 100 μm spacing between each turn. A larger ratio of the turn width to the gap between the lines, while maintaining the total actuator width, would also produce more force due to the increased combined Nitinol width; but there needed to be sufficient spacing between each turn to avoid electrical shorts. Four turns of the coil resulted in a total actuator width of 2.7 mm and an inductance of 57.5 nH. $SiO_2$ was chosen as part of the dielectric layer in the capacitor since it was already being used to stress the Nitinol; one deposition could serve two purposes. A layer of polyimide was added to the $SiO_2$ dielectric to fill in any possible pinholes in the oxide to prevent a short circuit between the electrodes. To remove the need for wire bonding between the coil and the capacitor, a copper layer was patterned to form a capacitor electrode and an electrical connection between the capacitor and the inner end of the coil; this completed the *LC* circuit as shown in Figure 3.3. $SiO_2$ was also selectively patterned beneath the interconnect to prevent shorting between the copper line and the Nitinol while the actuator is in motion. To balance out the stress caused by $SiO_2$ in the capacitor and on those small areas, the same amount of oxide was patterned on the back side of the Nitinol layer. With FEA, the 2-μm-thick $SiO_2$ and 2.64-μm-thick polyimide dielectric layer resulted in a capacitance of 15.0 pF (similar to the analytical value of 14.1 pF calculated from $C = \varepsilon A/d$ for a parallel plate capacitor); the actuator had a total resistance of 1.86 Ω. Using the equation $f_R = 1/\left(2\pi\sqrt{LC}\right)$, the resonant frequency is calculated to be 171 MHz which is in the desired range. When the actuator is exposed to an RF electromagnetic field with a frequency matching its $f_R$, it generates an ac electromotive force (EMF) most efficiently. The resulting ac current produces Joule heating directly in the coil and when its temperature passes the activation (austenite-phase) temperature, $T_a$, defined by the particular Nitinol composition, the coil returns to its remembered, flat shape. If the RF field is shifted to a frequency outside of the actuator's active range (Figure 3.3, defined by the range of field frequencies which cause the actuator to produce a temperature higher than $T_a$) or simply turned off, the actuator will cool down below $T_a$ and the Nitinol will return back to the martensite phase where it becomes compliant. The stress layer deforms the SMA

structure once again so that actuation can be repeated. Following the simulations, photomasks were designed in Tanner EDA L-Edit using the previously stated dimensions.

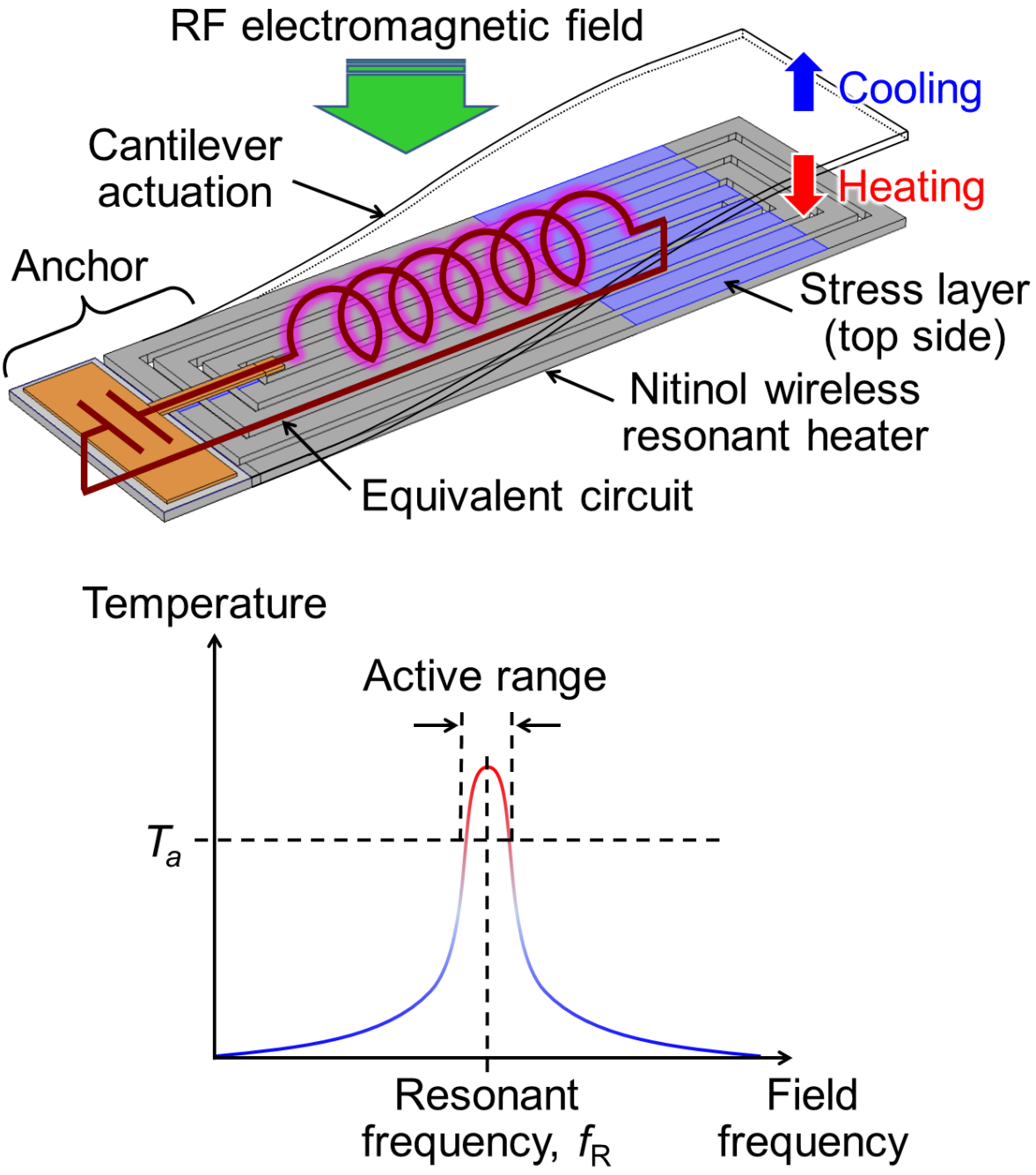


Figure 3.3: Conceptual diagram and working principle of the wireless, cantilever-like actuator based on a resonant Nitinol coil with an integrated capacitor

### 3.2 Pump Chamber and Reservoir

The entire device was built around the 9.2×2.7 $mm^2$ Nitinol actuator to have an overall size of about 10×10×2 $mm^3$. To maximize drug loading, the remaining space was set aside for the reservoir as shown in Figure 3.4.

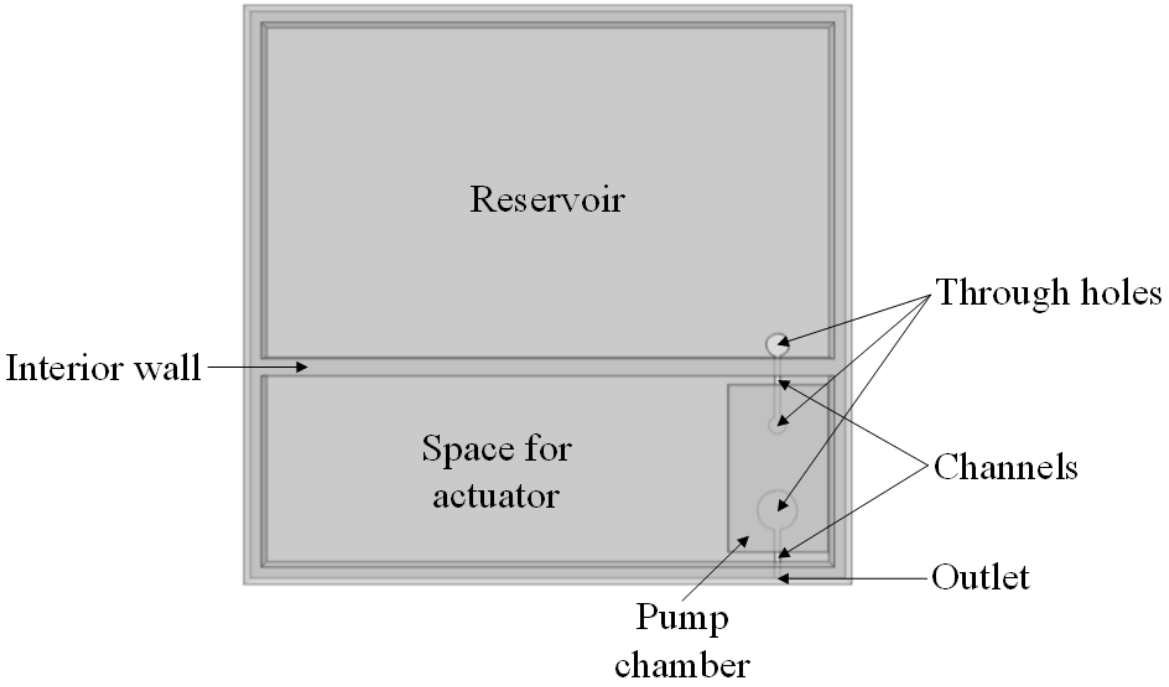


Figure 3.4: Pump chamber and reservoir of the drug delivery device

The pump chamber has to be beneath the free end of the actuator so it was placed at the bottom right corner. It was made to be 1.75 mm wide and 2.94 mm long. The height of the chamber has to be less than the displacement of the actuator (230 μm); but since the chamber would be formed by depositing Parylene over a block of sacrificial material, the height would be limited by the achievable thickness of the sacrificial layer.

The device walls were designed to be machined out of a 60-mil-thick (1.524 mm) sheet of polyimide. The exterior walls encase the entire chip and the interior wall separates the fluid in the reservoir from contacting the actuator. These 300-μm-thick walls are quite rigid to prevent the chip from collapsing due to possible external pressures. Because of the interior wall, a channel underneath it is required to connect the reservoir to the pump chamber. Another channel is also needed to bring the drug from the pump chamber to the exterior. The

channels would be created by wet etching through a 5-mil-thick (127 μm) substrate of polyimide; the top of the channels would be sealed with Parylene-C and the bottom side by bonding on another sheet of 5-mil-thick polyimide. Even though the polyimide etchant is isotropic, the smallest width of the channels will be ~100 μm.

In order for the fluid to be pumped directionally, out-of-plane check valves are created at the two through holes in the pump chamber (Figure 3.4) from two layers of the Parylene; one layer acting as the valve disc and the other as the valve seat. The inlet valve has the disc on the top layer whereas the outlet valve has it on the bottom layer. Four different valves were placed on the photomasks as shown in Figure 3.5. All of them had 500-μm-diameter valve discs and 300-μm-diameter holes in the valve seats. Valve (a) has 50-μm-wide and 100-μm-long tethers, (b) has 100-μm-wide and 100-μm-long ones, (c) has 30-μm-wide and ~230-μm-long ones, and (d) has 50-μm-wide and ~225-μm-long ones. These valve designs are similar to the ones previously reported in [22], [64] except the current design uses a thin layer of the Parylene as the valve seat rather than a thick, rigid substrate.

(a) (b) (c) (d)

Figure 3.5: Four valve designs with different sized tethers

The model of the fully packaged pump chamber and reservoir is shown in Figure 3.6. A 12-mil-thick (305 μm) polyimide piece is used to seal the top of the DDD, making the total device size 10.0×10.5×2.1 $mm^3$. A 0.8×0.8 $mm^2$ square hole is created in the cover for refilling purposes and is to be plugged during operation. This device design is considered to be implantable because, in addition to its small form factor, all components in contact with the human body and the drugs are made of polyimide or Parylene-C, both commonly used biocompatible materials.

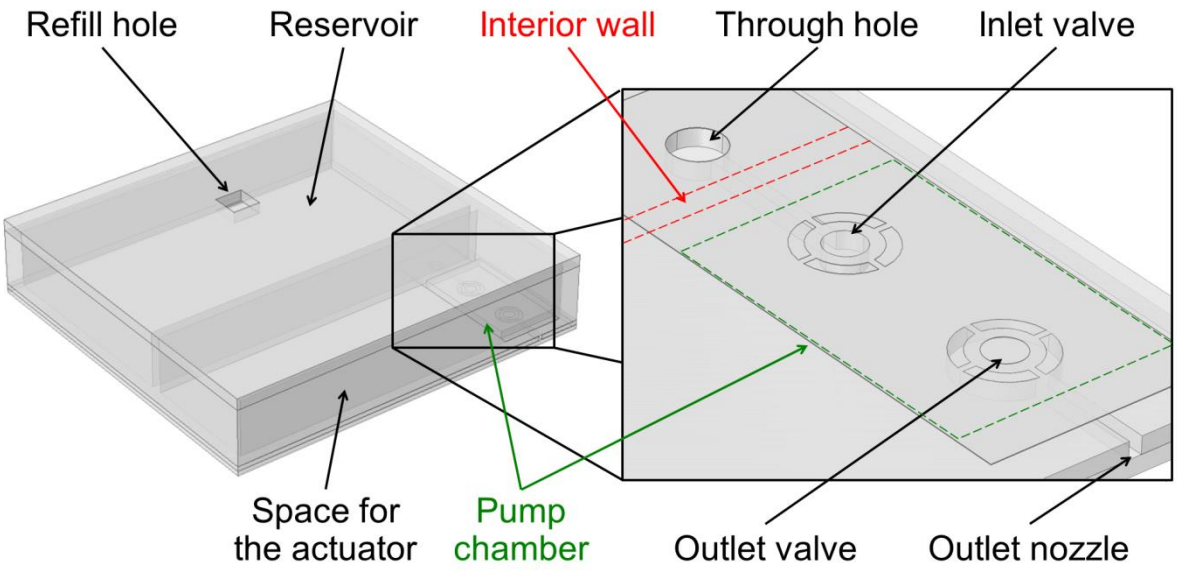


Figure 3.6: 3D model of the DDD (excluding the actuator) and a close-up view of the valves

# Chapter 4: Fabrication

The following chapter describes the steps involved with fabrication of the entire drug delivery device. Specific process parameters can be found in Appendix A.

## 4.1 Actuator

A planar piece of 200-μm-thick nickel titanium alloy (Alloy M, $A_s$ = 40 °C, $T_a$ (or $A_f$) = 65 °C, Memry) was thinned down to 100 μm using a wet etchant consisting of 10% hydrofluoric acid, 30% nitric acid, and 60% distilled water. With the Nitinol thinned down to the desired thickness, alignment holes were drilled through the sample to allow for accurate back side lithography. A μEDM machine (EM203, Smaltec) was used for all precise machining of the Nitinol samples. Two through holes were made using a tungsten electrode. Then the sample was ultrasonically cleaned with soap, acetone, and IPA to remove the EDM oil and debris. A 30 s descum was also performed using a PECVD machine (Minilock-Orion, Trion Technology) for cleaning. With the same machine, $SiO_2$ was deposited onto the Nitinol; after heating the reactor chamber to 290 °C, the sample was loaded and 2 μm of $SiO_2$ was deposited over 30 min. Then the sample was flipped over and the other side received another 2 μm of $SiO_2$.

In order to pattern each $SiO_2$ layer independently using wet etchant, the other side had to be protected. SPR220-7.0 positive photoresist (Rohm and Haas Company) was deposited onto a glass substrate using a spin coater. The Nitinol sample was placed onto the wet photoresist and baked on a hotplate at 115 °C for 5 min to adhere it and to protect the $SiO_2$ on the underside from the etchant. To pattern the top $SiO_2$ layer, a 1.5-μm-thick layer of S1813 positive photoresist (Rohm and Haas Company) was spun on. The sample was exposed using an MJB-3 mask aligner (Karl Suss) and then developed. The excess space on the substrate surrounding the actuator was masked off to prevent etching of $SiO_2$ in the areas that did not matter. This reduces the curvature of the sample after etching, making it easier for subsequent processing. The sample was submerged in buffered oxide etchant for 20 min to pattern the top $SiO_2$ layer. The mask was then removed and all the photoresist was washed away using acetone and IPA. The sample had a slight curvature due to the stress of the oxide on only one side. It was flipped over and bonded onto another glass substrate using SPR220

again. Bonding it not only protected the patterned oxide but also kept the sample flat. The baking temperature was higher than $T_a$ so the Nitinol flattened out while the photoresist solidified, keeping the sample flat even when cooled down. The $SiO_2$ layer on the back side (now facing up) was patterned in the same way as the top side; photolithography with S1813 was used to define the features, the outer areas were masked off, $SiO_2$ was etched, and the sample was separated from the glass substrate. Now the sample was relatively flat since both sides had similar amounts of oxide.

Flipping the sample over again (top side facing up) and masking off the area surrounding the capacitor, the surface was descummed and a polyimide precursor (HD-3007, HD Microsystems) was spun on as a dielectric layer. After soft baking and removing the mask, the polyimide was cured at 300 °C to produce a 2.64-μm-thick layer, according to its data sheet [67]. The sample was adhered to a glass substrate and S1813 was patterned to define the areas for metal deposition. Next, 15 nm of titanium followed by 150 nm of copper was deposited using an electron beam evaporator (Airco-Temescal). Then a 37-μm-thick negative dry film photoresist (PM240, Dupont) was applied using a hot roll laminator. The photoresist was exposed then developed to form an electroplating mold, after which 30-40 μm of copper was electroplated in the mold to thicken the capacitor electrode and to form the bridge connecting the capacitor to the inner end of the coil. Afterwards, the PM240 was stripped off using 3% potassium hydroxide which also dissolved the SPR220 and lifted off the excess evaporated metal layer. The sample was flipped over and bonded onto a glass substrate one final time. With the copper bridge on the underside, the Nitinol was finally micromachined into the designed coil shape using μEDM and then released from the substrate for final cleaning.

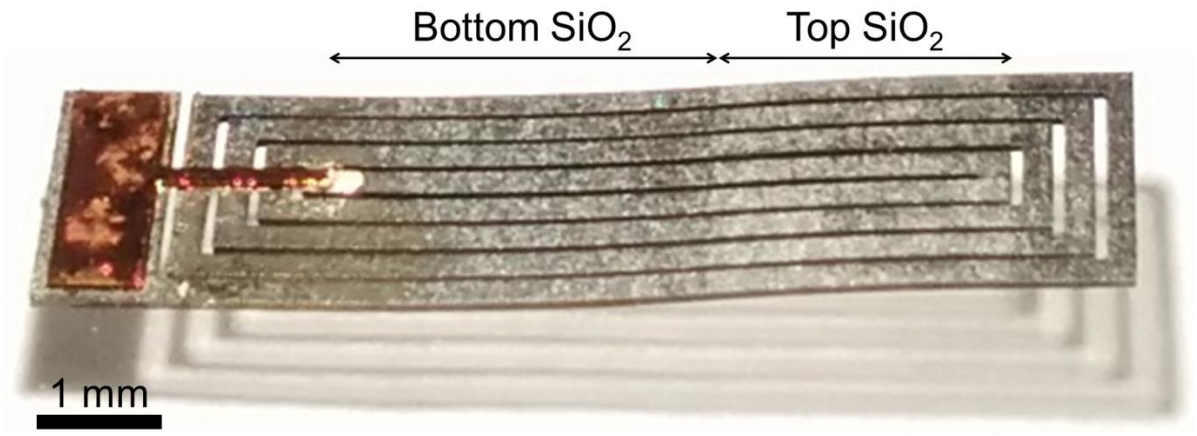


(a)

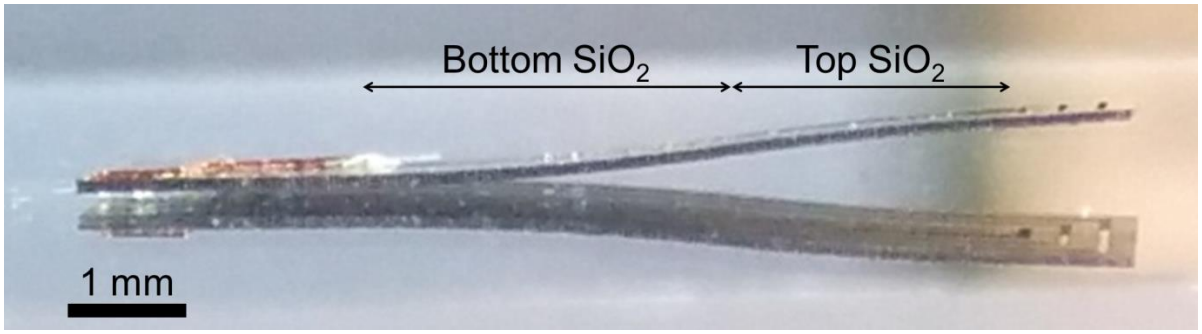


(b)

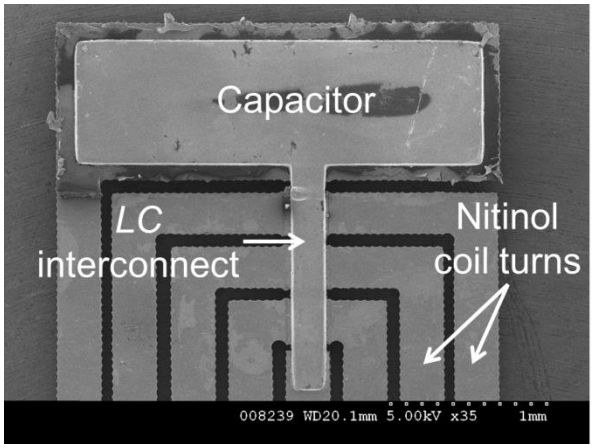


(c)

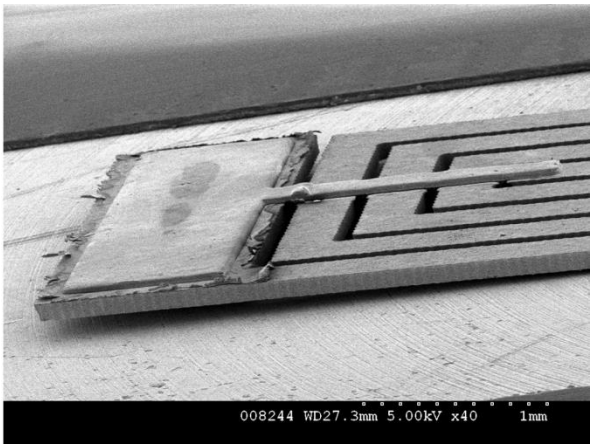


(d)

Figure 4.1: Fabricated actuator in the martensite state on a glass substrate with (a) an angled view and (b) a side view showing the displacement of the cantilever-like structure. (c) and (d) Scanning-electron-microscope images of the completed actuator showing its capacitor end

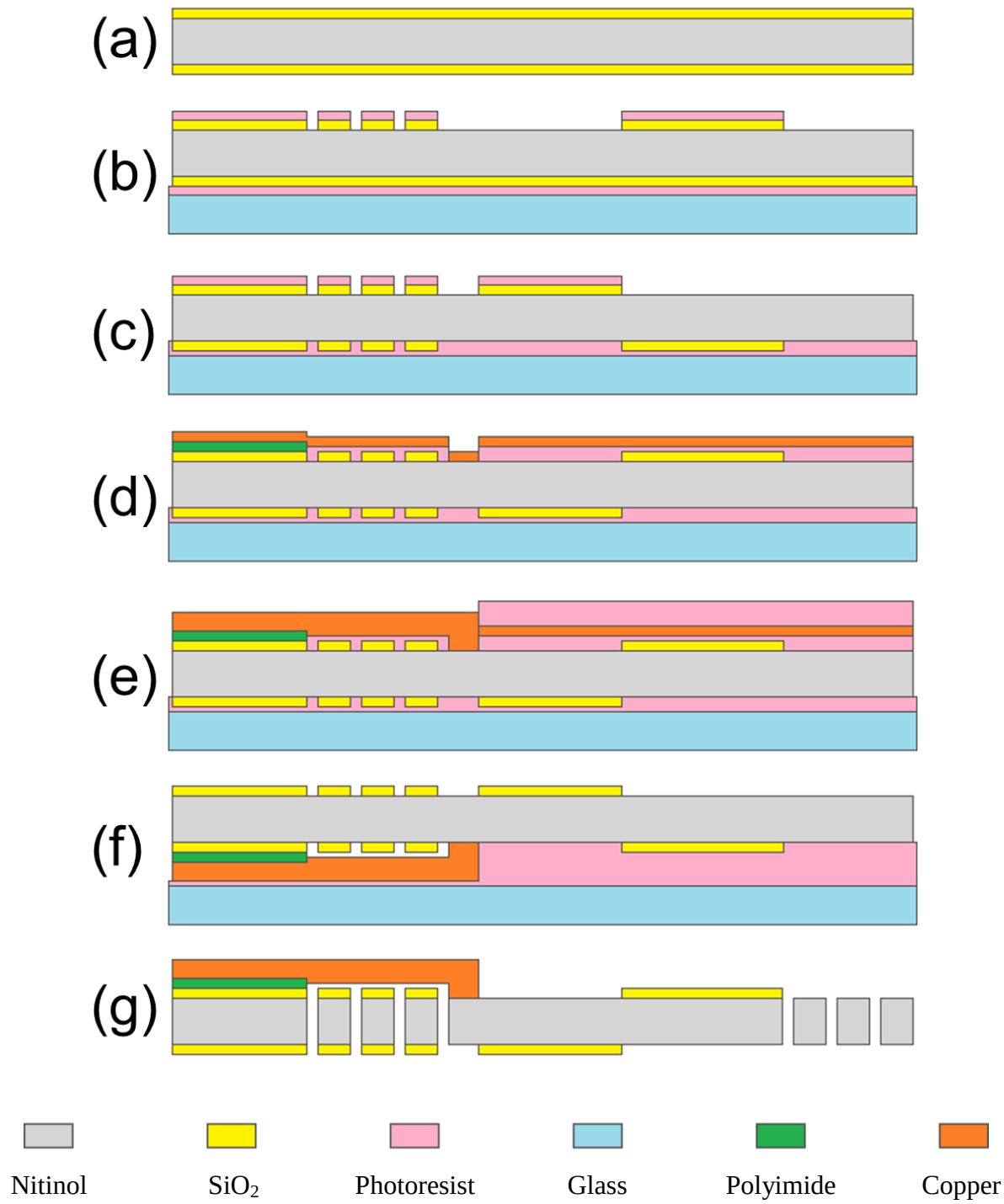


Figure 4.2: Actuator fabrication process flow (not to scale). (a) Thin down Nitinol and deposit $SiO_2$ onto both sides; (b) pattern top oxide; (c) pattern bottom oxide; (d) deposit polyimide and Ti/Cu seed layer; (e) electroplate thicker layer of copper; (f) flip over and bond to a glass substrate; and (g) machine out coil shape using µEDM and release from glass

### 4.2 Pump Chamber and Reservoir

A piece of 5-mil-thick polyimide film (Fralock) was cut out and cleaned with acetone and IPA. Next, 3 μm of Parylene-C was deposited onto both sides of the substrate using a Parylene deposition system (PDS 2010 Labcoter 2, Specialty Coating Systems). Then 7-μm-thick SPR220 was spun on, soft baked, and exposed. After post-exposure baking, the photoresist was developed with MF-24A (Rohm and Haas Company) and the sample was placed in the Trion PECVD machine for an oxygen plasma etch. This dry, anisotropic etch was used to pattern through the Parylene layer with the photoresist as an etch mask. After all the remaining SPR220 had been washed off, S1813 was spun on to the top side, over the patterned Parylene features; then the sample was exposed and developed; this photoresist layer was used as a spacer to prevent the valve disc on one Parylene layer from bonding with the valve seat on the other layer. Then Kapton tape was used to seal all the edges of the polyimide substrate to a silicon wafer. The surface was descummed and another 3 μm of Parylene was deposited; the tape prevented the back side from receiving any Parylene vapor during the deposition. The second layer of Parylene was patterned the same way as the first layer; photolithography was performed using SPR220 to form an etch mask, the Parylene was etched through using $O_2$ plasma, and the remaining photoresist was removed with acetone and IPA. Fabrication of the check valves was complete. Etching past the first Parylene layer was not much of a concern since the polyimide underneath would later be etched via wet chemistry; but controlling the etch depth of the second Parylene layer was important because over etching would ruin the features in the first layer.

Next, the sample was flipped over and the Parylene on the back side was patterned to form an etch mask; this defined where on the substrate the polyimide etchant could react with to etch out the microfluidic channels and the through holes. The sample was flipped over again to add a ~200-μm-thick sacrificial layer for the pump chamber. Although a thick layer of photoresist (160-180 μm) could be attained by spinning on several coats of SPR220 at low speed for a short duration, the resultant film becomes too opaque; mask alignment was difficult. Instead, a small amount of SPR220 was manually applied on the pump chamber area. The sample is then baked on the hot plate at 75 °C for 3 hours, followed by gradual cooling. Since the alignment marks were not covered by photoresist, it was possible to

perform accurate photolithography. Due to the layer's large thickness, a long exposure time was required. To circumvent an extremely long exposure that leads to thermal damage (bubbling) of the photoresist, it was repeatedly exposed (with shorter intervals) and developed until all the excess photoresist was removed. After the photoresist was fully patterned into a ~170-μm-thick block, the substrate edges were taped onto a wafer to prevent Parylene deposition on the back side again.

A quick 30 s descum was performed to clean the surface while avoiding bubbling of the photoresist which is due to the heat and the vacuum in the reactor chamber. Then 5 μm of Parylene was coated onto the top side of the substrate. Now there was Parylene covering the entire substrate except for the etched patterns on the back side. The sample was removed from the wafer and then the exposed areas on the polyimide substrate were wet etched to form the channels leading from the reservoir to the inlet valve and from the outlet valve to the exterior of the device. The polyimide etchant contained 40% potassium hydroxide, 20% ethanolamine, and 40% distilled water and was heated to 87 °C [68]. Because of the small channel widths, an ultrasonic bath was used to assist the etching process. The device was then rinsed with hot water. With the channels etched into the polyimide as shown in Figure 4.3, removal of the sacrificial layer with acetone was possible. Once all the photoresist was flushed out of the pump chamber, IPA followed by hot water was pumped through it to remove the organic solvents.

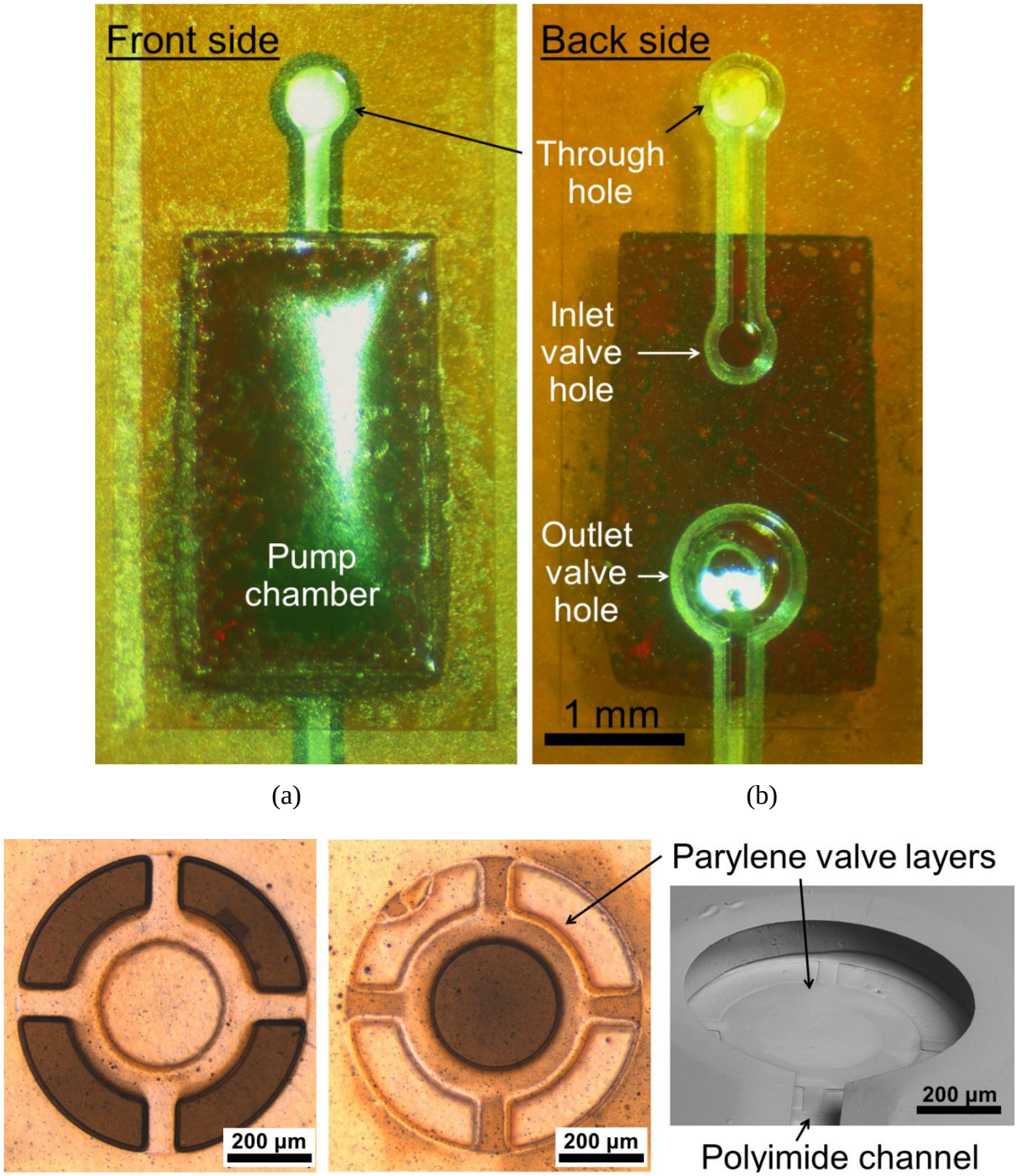


Figure 4.3: (a) Front side and (b) back side of the microfluidic channels and Parylene pump chamber created in/on the polyimide substrate; (c) inlet valve with the valve disc on top, (d) outlet valve with the valve seat on top, and (e) scanning electron microscope (SEM) image of an outlet valve formed on the polyimide channel structure

The walls of the final device were mechanically micromachined out of a 60-mil-thick piece of polyimide (Fralock) using the Smaltec EM203. The drill bit machined through the entire depth of the polyimide along the edges of 3 rectangles, one for the actuator, another for the reservoir, and a final one surrounding the previous two. The two interior blocks were removed to produce the piece shown in Figure 4.4 with exterior walls and an interior wall to separate the actuator and pump chamber from the reservoir.

A piece of 5-mil-thick polyimide was bonded with the two previously made components. HD-3007, which also acts as an adhesive, was spun onto the new polyimide piece at 3000 rpm for 30 s and baked on a hotplate at 100 °C for 5 s. This brief soft bake was to dry the adhesive slightly to prevent it from filling in the channels and blocking fluid flow. The piece containing the pump chamber was then placed on top of the adhesive. More HD-3007 was applied to the bottom side of the walls and then placed on to the pump chamber piece. ~40 kPa was applied to the combined device while baking at 100 °C for 30 min to bond the three pieces together. Afterwards, a through hole was punctured into the 5-μm-thick Parylene to connect the reservoir to the underlying channel.

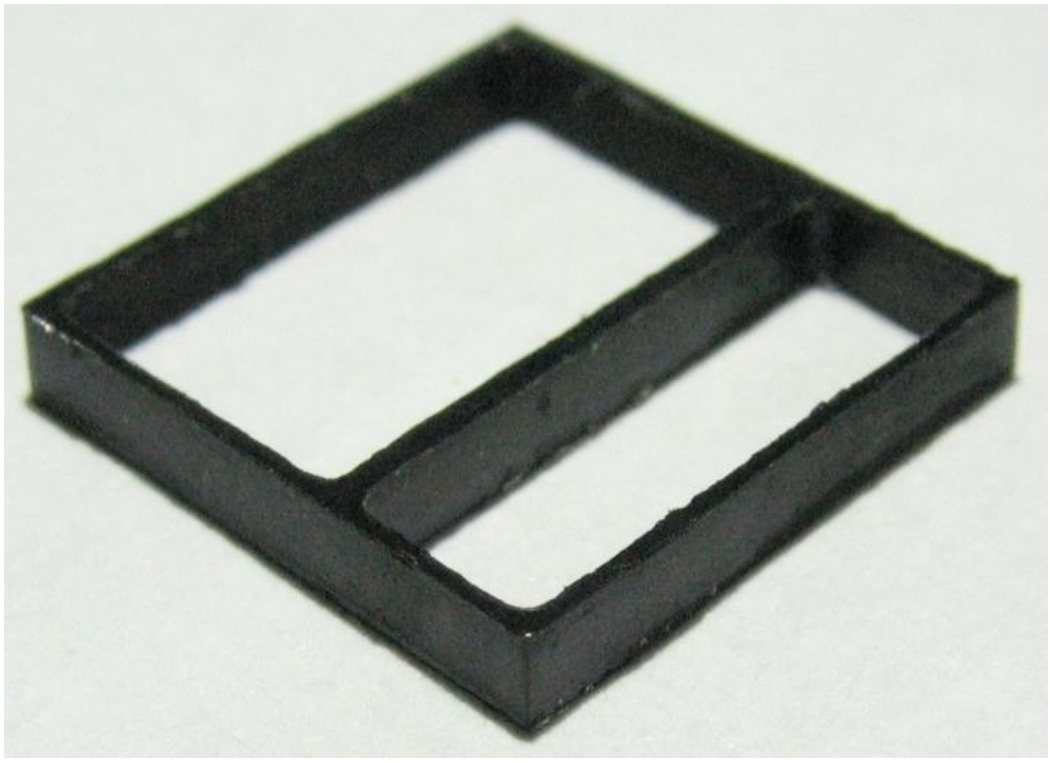

Figure 4.4: 60-mil-tall polyimide walls for the DDD

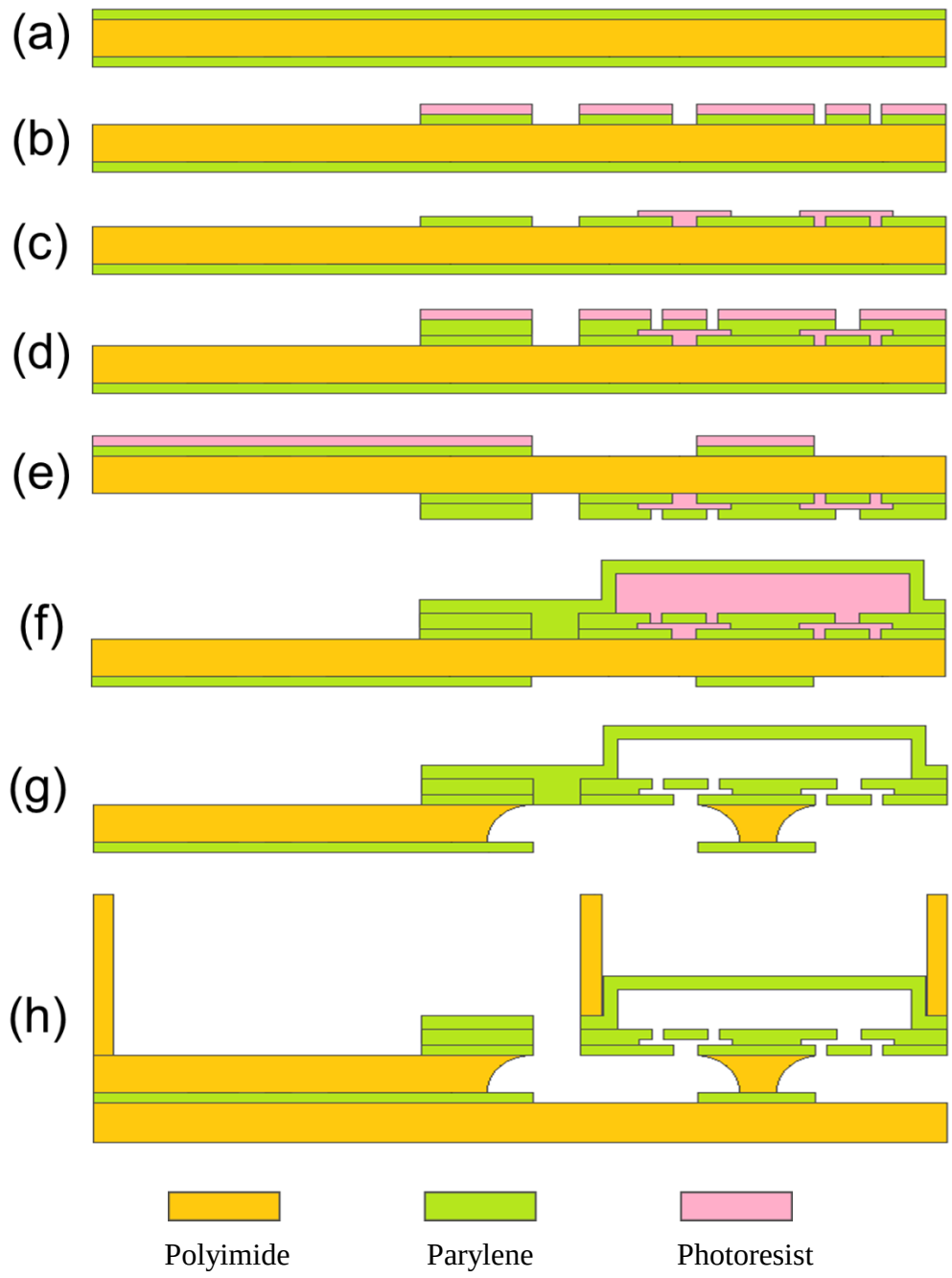


Figure 4.5: Pump chamber and reservoir fabrication process flow (not to scale). (a) Deposit Parylene onto both sides of the polyimide substrate; (b) pattern top side Parylene layer; (c) deposit photoresist spacer layer; (d) deposit Parylene onto top side and pattern; (e) pattern back side Parylene layer; (f) deposit and pattern sacrificial photoresist and deposit Parylene onto top side; (g) wet etch channels into polyimide and remove sacrificial photoresist; and (h) make a through hole and bond to the device walls and another polyimide layer

### 4.3 Complete Device

Two small pieces of 12-mil-thick polyimide (Fralock) were cut out and bonded onto the bottom side of the actuator. One piece was bonded at the capacitor end and another piece at the free end using HD-3007 adhesive at 125 °C for 15 min. The polyimide at the free end was used as a thermal barrier between the actuator and the pump chamber to minimize heating of the pumped out fluid. The other piece was to raise the fixed end by the same height. More HD-3007 was applied to the bottom side of the polyimide spacers and then the actuator was placed in its designated spot; it was bonded in place by heating the entire device to 100 °C for 10 min. This fixed the capacitor end to the base of the device and the free end to the top of the pump chamber. Then the excess polyimide substrate protruding past the device walls was cut off. Using the μEDM system, a 10×10.5 $mm^2$ piece of 12-mil-thick polyimide, with a 0.8×0.8 $mm^2$ square refill hole, was made to fit exactly over the device walls; then it was bonded on as shown on the right of Figure 4.6(a).

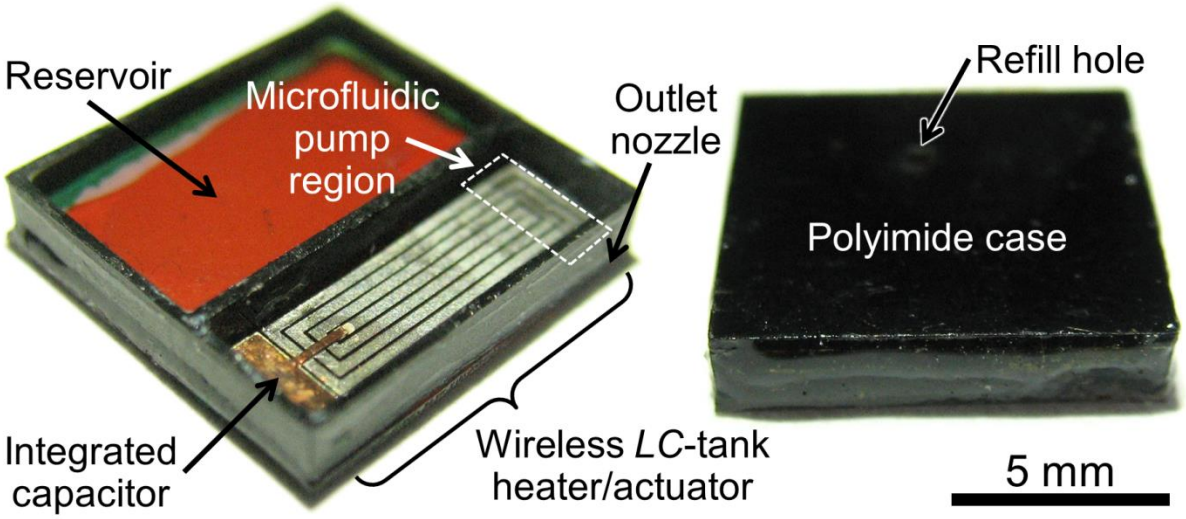


(a)

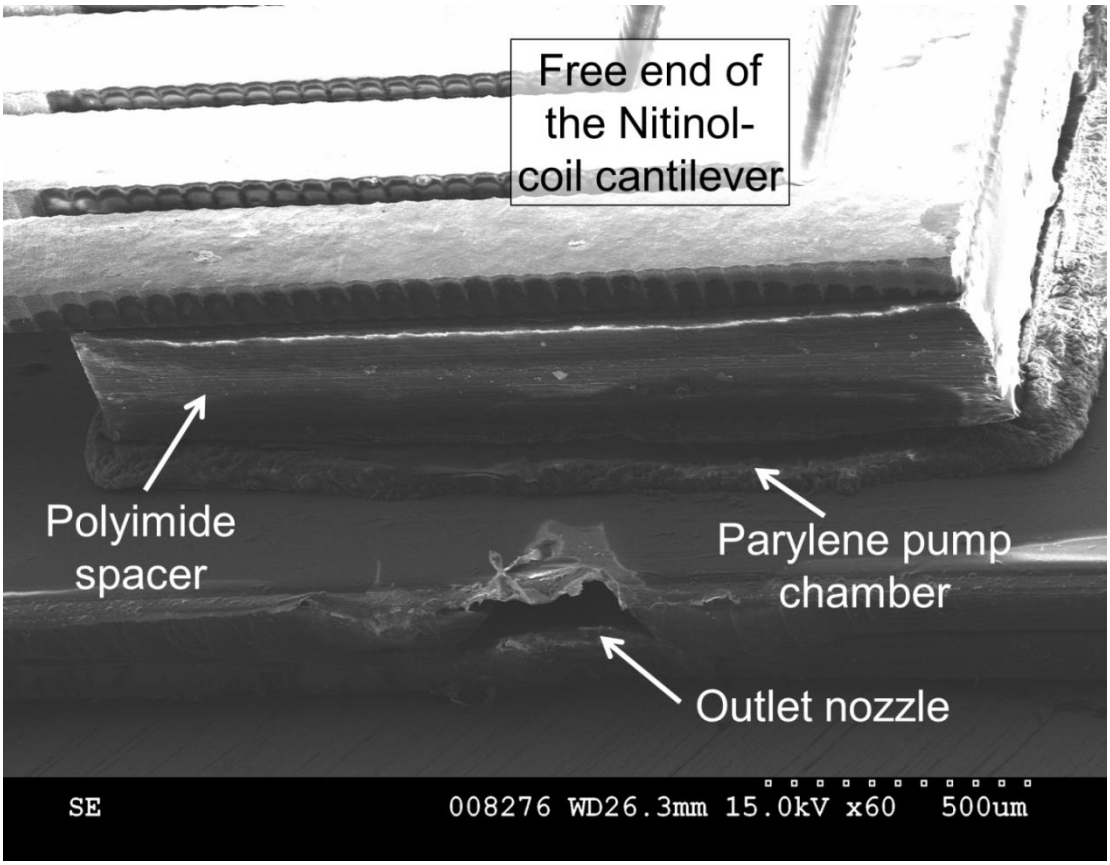


(b)

Figure 4.6: Completed DDD chip (left) without and (right) with the top cover; (b) close-up SEM image of the integrated Nitinol actuator coupled with the pump chamber

# Chapter 5: Results and Discussion

## 5.1 Actuator

A copper coil (with four turns, a rectangular form, and a size comparable to the actuator) was used as an external antenna and connected to an impedance analyzer (4396B, Agilent Technologies) for wireless testing of the fabricated actuators. The actuator was placed directly above the antenna to inductively couple them together. By looking at Figure 5.1, the phase dip determines the resonant frequency to be 167 MHz which strongly agrees with the COMSOL simulation of 171 MHz.

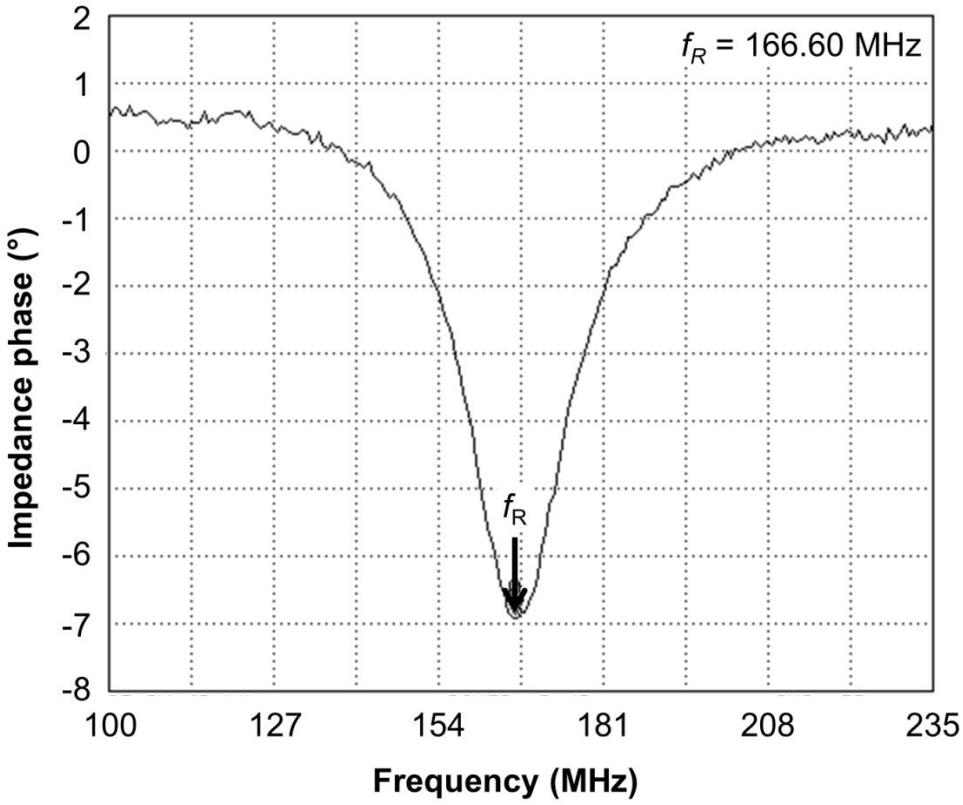


Figure 5.1: A phase dip recorded in the impedance of the external coil antenna inductively coupled with the actuator indicating its $f_R$ of 167 MHz

A fabricated actuator without the capacitor-coil interconnect was directly connected in series to the analyzer using a wired interface to evaluate the inductive and capacitive components of the device. The actuator was modeled as a series *RLC* circuit using the

equivalent circuit function in the analyzer and it calculated that capacitance = 11.2 pF, inductance = 59.8 nH, and resistance = 12.0 Ω. The inductance agrees very well with the COMSOL simulation of 57.5 nH. The capacitance was less than 15.0 pF due to the thicker dielectric layer, and the extra resistance can be attributed to the contact resistance in the wired interface. Probing only the inductor, the inductance, *Q*-factor, and resistance of the coil over a range of frequencies are shown in Figure 5.2. The inductance at its resonant frequency matches the value determined by the equivalent circuit model. The coil's *Q*-factor had a peak of ~7.5 at ~230 MHz, slightly higher than the measured $f_R$ (194 MHz) of the actuator. The increase in the parasitic resistance with frequency is presumably caused by the skin effect induced in the coil.

Then the heating profile of the first actuator was examined using the experimental set-up shown in Figure 5.3. The signal from an RF signal generator (HP8657A, Hewlett Packard) was amplified with a power amplifier (TIA-1000-1R8, Mini-Circuits) to produce RF electromagnetic fields using the transmission coil antenna. An amplified RF output power of up to 1.1 W was used for testing. The actuator was aligned and located in proximity (distance ~1 mm) to the external antenna in these tests. An infrared (IR) camera (VarioCAM HiRes research 1.2 Mega, Jenoptik) was used to observe the actuator from above. Using the resonant frequency recorded from the impedance analyzer as a starting point, frequencies around this value were tested; it was found that 170 MHz produced the highest temperatures rather than 167 MHz. This can be explained by the fact that the analyzer measures the resonant frequency of the actuator in its cold state whereas RF testing looks at the actuator in its hot state. The slight deformation between the two phases causes a change in its inductance, thus altering the resonant frequency. And 170 MHz agrees even better with the COMSOL simulation of 171 MHz since it was modeling a completely flat actuator, in other words, the hot state.

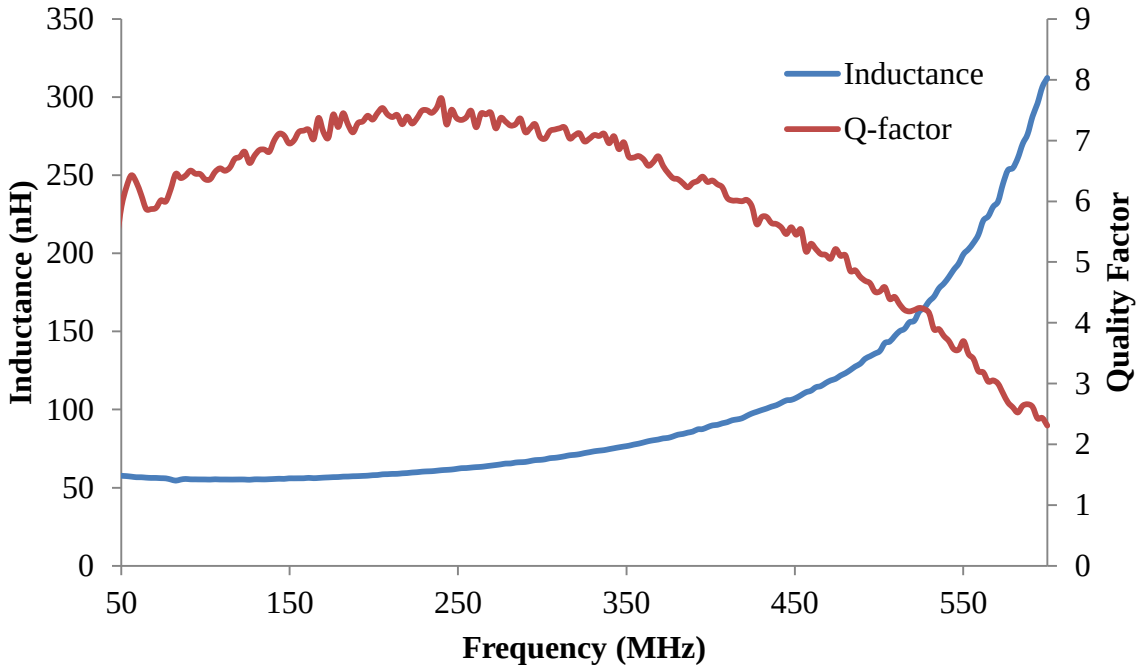


(a)

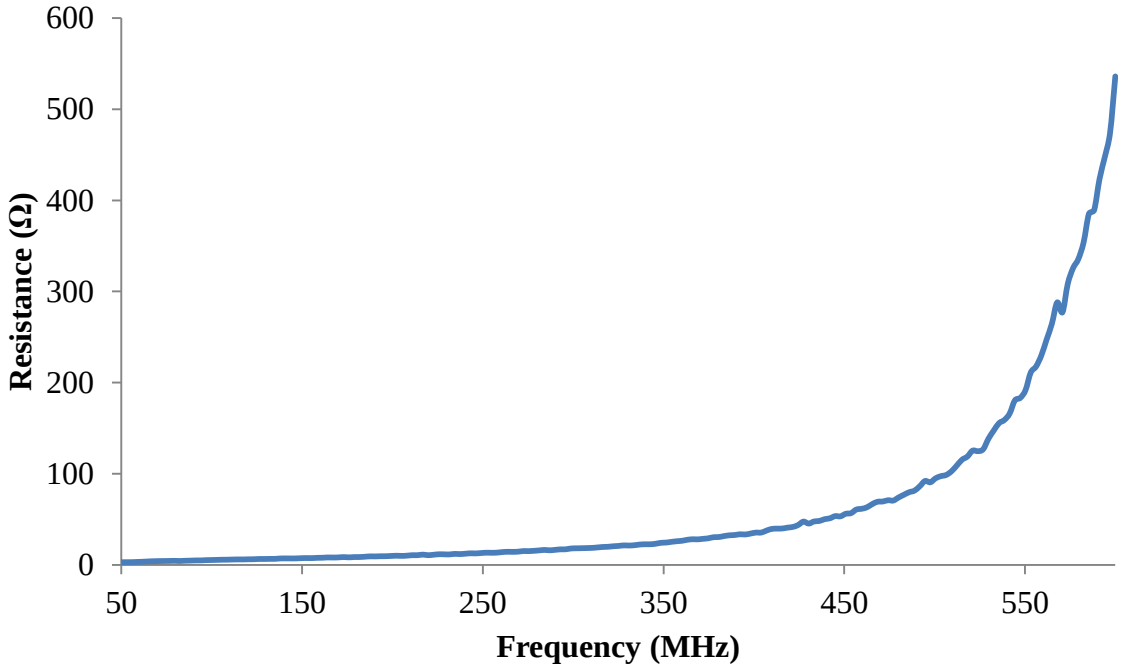


(b)

Figure 5.2: Characteristics of (a) inductance, *Q*-factor, and (b) parasitic resistance of the fabricated actuator device measured as a function of frequency through a wired interface

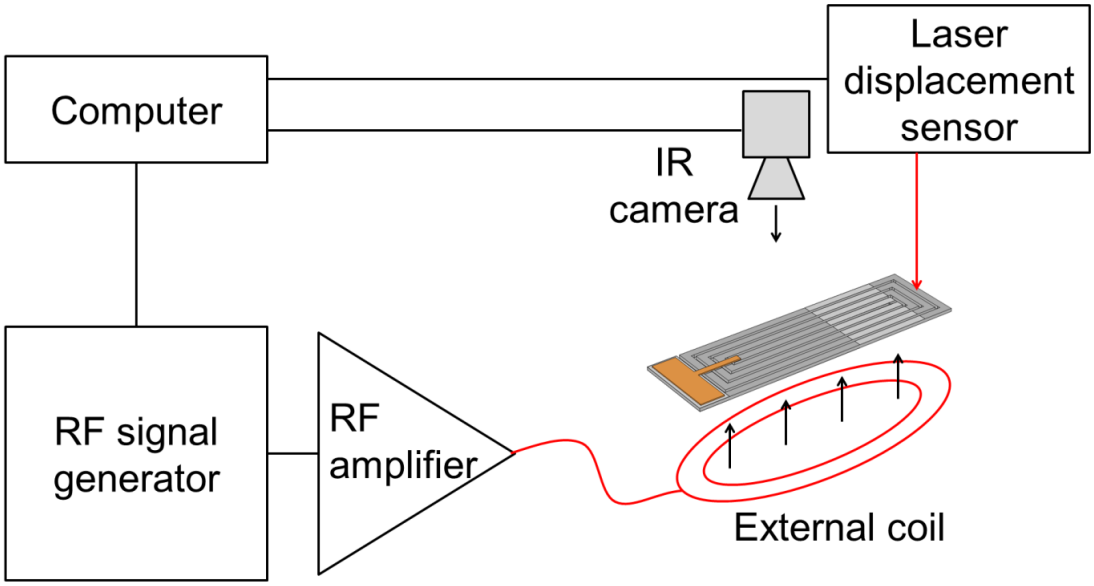


Figure 5.3: Experimental set-up used for wireless RF heating and actuation tests of the fabricated actuators

Using an output power of 0.66 W, the actuator was able to hit 80 °C within 20 s as shown in Figure 5.4(c). But only the innermost coil turn reached that temperature; the further away the turn, the cooler it was. In this case, the two inner turns of Nitinol should have fully changed from martensite to austenite (temperature greater than $T_a$) but the two outer turns would not have. The temperatures of the inner turns were found to be consistently higher than those of the outer turns; this effect is likely caused by a non-uniform magnetic-flux distribution within the coil (higher towards its center) [69] (also reported with a previous actuator design [60]). Due to the presence of the transitional state between the martensite and austenite phases (this particular Nitinol composition has $A_s$ = 40 °C and $A_f$ = 65 °C, equivalent to $T_a$ as defined before), temperatures between $A_s$ and $T_a$ do not result in a full transition to the austenite phase but the material still contains a percentage of it. And as a result, those turns should still produce a (smaller) displacement.

Note that the measured regions are where the $SiO_2$ layer is located. It appears that the bare Nitinol was lower in temperature and that the copper did not really heat up, but this is not true. The temperatures displayed by the IR camera are very dependent on the emissivity of the material; in general, metals are inefficient at emitting infrared radiation and have low emissivity. The emissivity values can used to correct for the temperature readings but large

corrections are often unreliable [70]. So rather than recording the temperature of the Nitinol, the oxide was chosen and its (high) emissivity was used for imaging.

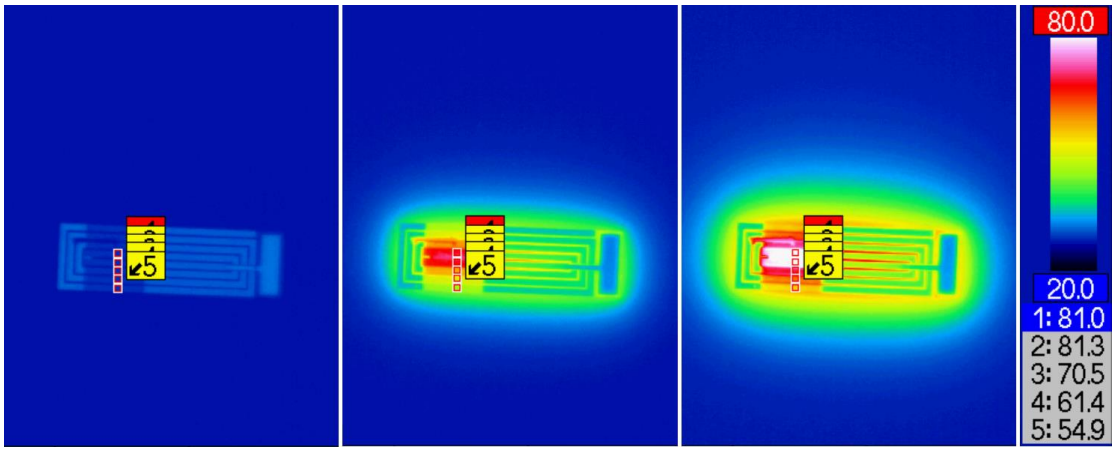


(a) (b) (c)

Figure 5.4: 170 MHz RF heating of the Nitinol actuator with 0.66 W at (a) 0 s, (b) 10 s, and (c) 20 s. Numbers 1-5 located in the legend correspond with the spots on the actuator with 1 at the top in ascending order

Due to a small change in the capacitance (caused by accidental contact of a chemical that could have affected the capacitor's dielectric layer), the field frequency producing the highest temperature shifted slightly from 170 MHz to 185 MHz – this modified resonant frequency was verified through the phase-dip detection method as well. The new frequency response of the actuator is shown in Figure 5.5; the reported temperatures were obtained from spot-1 in Figure 5.6. The RF field was turned on for 10 s then the actuator was allowed to cool for 20 s before the next frequency was activated. Figure 5.6 also shows the thermal response of different coil turns with the RF field on for 15 s and an output power of 0.78 W. Even with the actuator's center turn at 100 °C, the outermost turn only reaches 56 °C, which is higher than $A_s$ but lower than $T_a$. Similar measurements were made at varying RF powers and the peak temperatures for each of the different powers are plotted in Figure 5.7. With an output power of 1.1 W, even the outermost turn was able to pass $T_a$; however, with such high power, the innermost turn reaches nearly 150 °C. Large heat stress due to repetitive actuation could be a source of premature failure, shortening the device's longevity. In addition, the hotter the actuator gets, the longer it takes to cool down, resulting in longer cycling times.

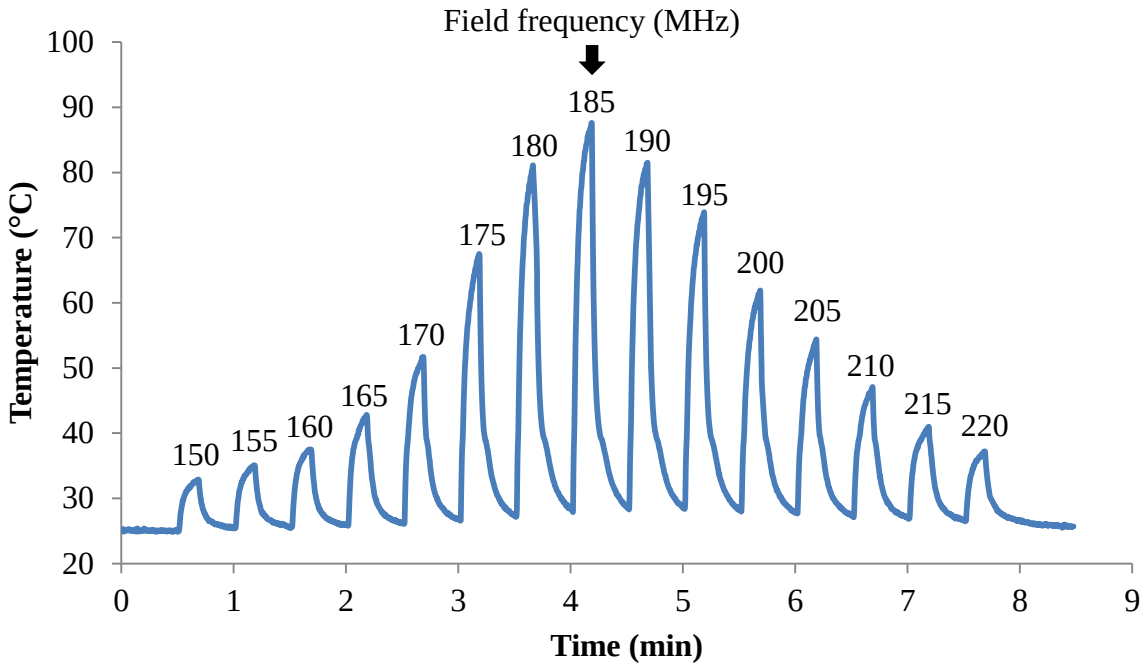


Figure 5.5: Thermal response of a fabricated actuator with a $f_R$ of 185 MHz to temporal wireless excitation at 0.60 W with varying frequencies; temperature was probed at the center region of the Nitinol coil

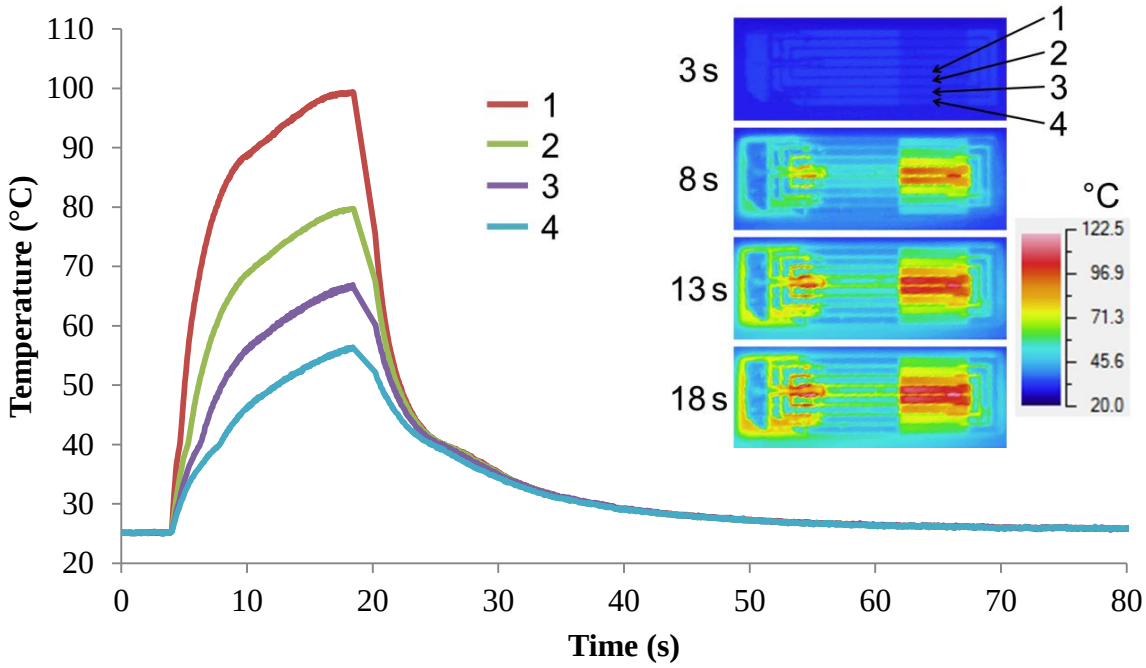


Figure 5.6: Temporal thermal responses for different coil turns excited using an RF output power of 0.78 W at 185 MHz

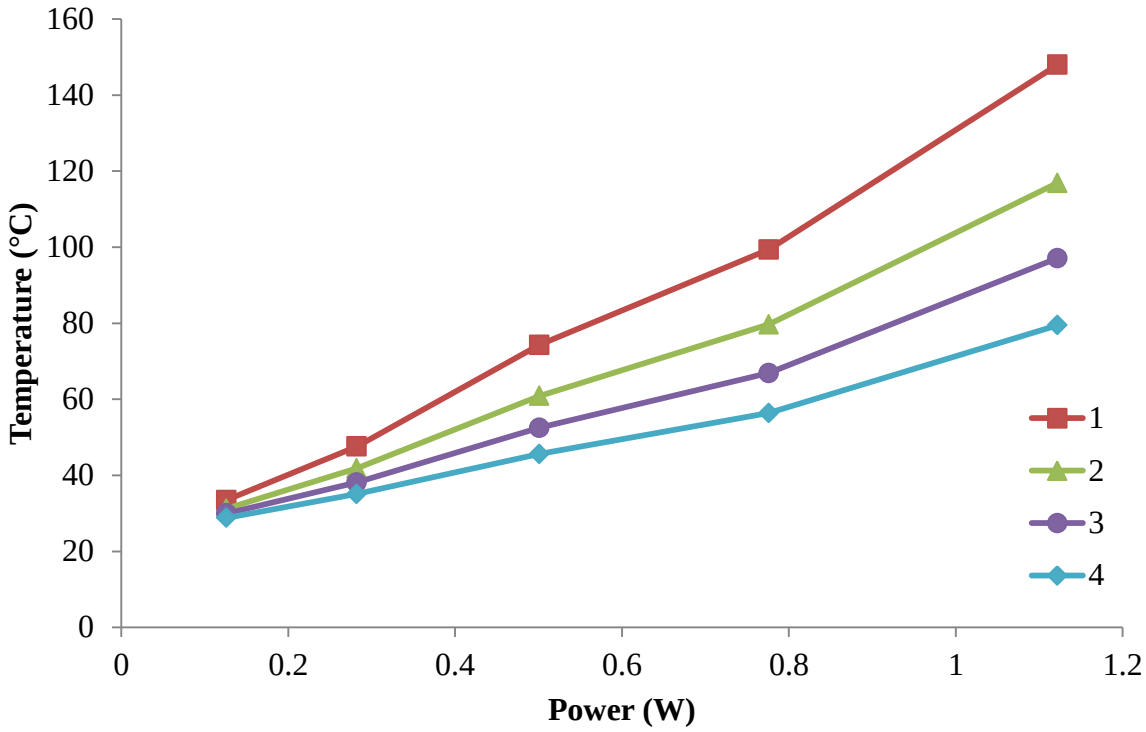


Figure 5.7: Maximum achieved temperature of different turns at 185 MHz after 15 s over a range of RF powers

Next was to measure the displacement of the actuator's free end (with the capacitor end anchored) during heating and cooling. With the antenna beneath the actuator, a laser displacement sensor (LK-G32, Keyence; sensing resolution 10 nm) was used to record the movement. The laser was aimed at the end of the coil turns and a 0.50 W RF field was turned on for ~20 s to produce the graph shown in Figure 5.8. The displacements sharply shot up immediately after the radiation was turned on and started saturating until the field was turned off, after which the displacement dropped off quickly but slowed down (at around 60 µm of displacement) as heat dissipated from the actuator. The result indicates that the innermost coil turn reached 160 µm (84% of the full displacement) within ~1.5 s, comparable to the speed reported with the non-cantilever design in [60] with half the RF power. The outermost turn reacted slower to the RF field but reached a slightly greater displacement (194 µm) than the innermost turn. It is also visible that the outermost turn exhibited faster return than the innermost one when the RF was turned off. The spatial distribution of heat in the coil (Figure 5.4) can explain these differences in mechanical response, i.e., the innermost turn displaces

faster due to more heating but returns to the cold state slower because it is surrounded by hot outer turns. It is worth noting that the discontinuities seen in the displacements after turning the RF on for ~1.5 s are likely related to an overshoot of RF power with the system used.

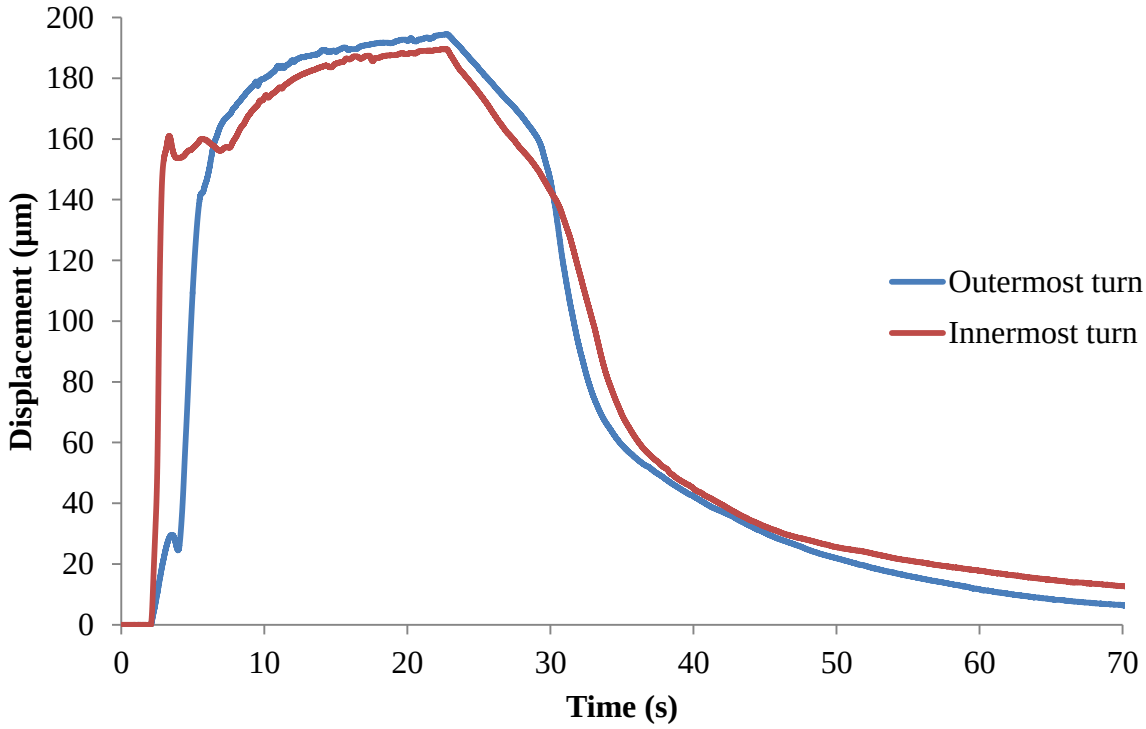


Figure 5.8: Temporal behavior of the displacement produced at the device's free end with the RF field activated for 20 s

The effect of field frequency on the actuation displacement was characterized using another device (with a thicker dielectric polyimide layer, resulting in $f_R$ = 245 MHz). The RF signal was turned on for 5 s then the actuator was allowed to cool down for 30 s before the next frequency was activated. The resulting displacements are plotted in Figure 5.9 with a peak of 215 µm.

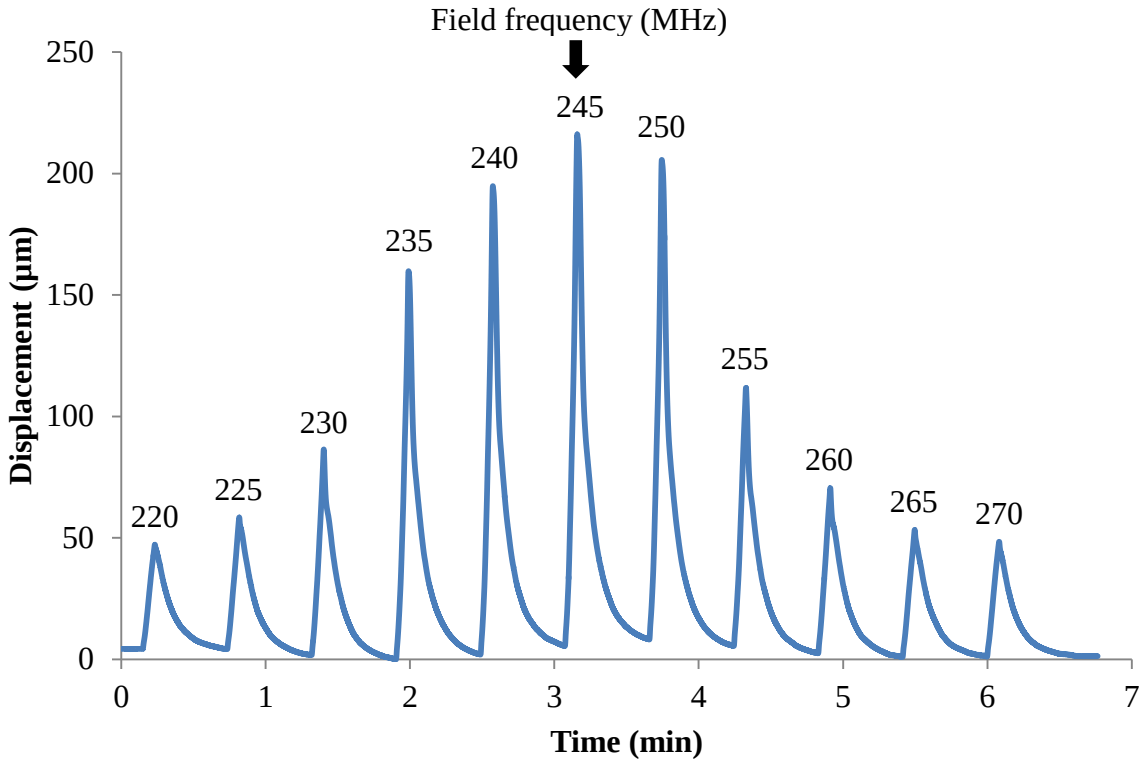


Figure 5.9: Frequency dependence of actuation displacement recorded under temporal excitation at different field frequencies surrounding the device's $f_R$ (245 MHz)

The force generated by the actuator was measured using a digital force gauge (DS2-1, Imada) as shown in Figure 5.10. The ends of all longitudinal coil turns on the capacitor side were fixed on a substrate as an anchor and the ends on the other side were in contact with the gauge's probe so that every coil line contributed to the total force produced. The maximum force in this setting (under RF excitation with an output power of 0.78 W at resonance) was measured to be 71 mN. The change in measured force over a range of field frequencies surrounding the device's $f_R$ (Figure 5.11) also clearly indicates the actuator's frequency dependence.

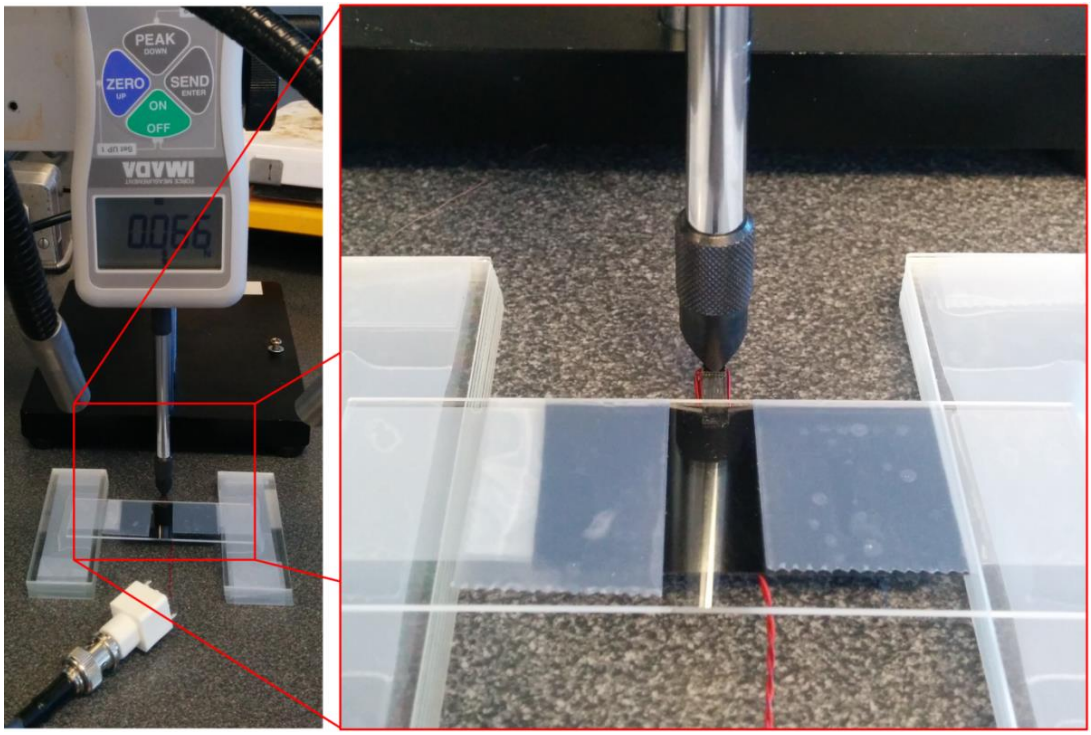


Figure 5.10: Set-up of the force gauge, the anchored actuator, and the external coil

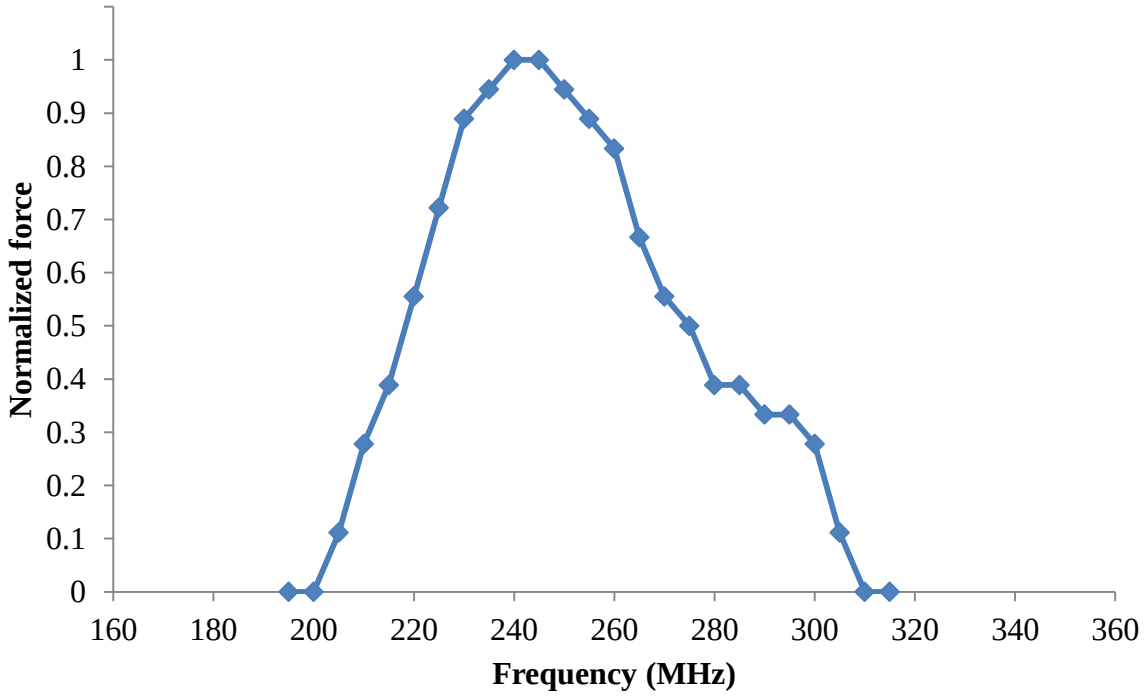


Figure 5.11: Normalized vertical forces generated at different field frequencies surrounding the device's $f_R$ (245 MHz) verifying that the maximum force is achieved at resonance

The observed maximum force of 71 mN is more than twice the force obtained from the self-heating SMA coil actuator in [60]; however, it is much less than the normal cantilever actuator reported in [44]. There are various sources for this outcome and some are related to the specific design of the current device. Comparing the regular unpatterned cantilever in [44] and the current coil cantilever, both actuators used the same Nitinol thickness but the combined width of the coil turns in the current cantilever results in a total width less than half of the other one. Also, the entire length (5 mm) of the unpatterned cantilever was covered with the oxide stress layer, hence the full length of the cantilever contributed to force generation when heated. In contrast, the current coil cantilever has shorter oxide on the bottom (3.25 mm); thus less SMA is at work to generate a downward force during heating. In addition, the top oxide actually negatively impacts the force generated downwards (the SMA in this stress region generates upward displacements and thus lowers the downward force). This oxide arrangement was effective in adjusting the profile of the cantilever to bring the free end nearly parallel with the substrate; however, this is indeed a trade-off with the produced force as observed in this experiment. This suggests that if the force is of particular interest for a certain application, one could redesign the profile adjustment or simply eliminate it, i.e., covering the entire bottom side with oxide and removing the top oxide layer to maximize the force.

### 5.2 Pump Chamber and Reservoir

The next set of tests was done to analyze the performance of the fabricated pump chamber by measuring the volume of fluid being pumped out. The device was surrounded by distilled water and the reservoir was filled with 10% sodium chloride. Using an electrical conductivity (EC) meter (HI 87314, Hanna Instruments), the change in conductivity of the surrounding water was measured and related to the amount of released salt. Compression and expansion of the chamber was carried out using a 3-axis stage with three stepper motor drives (MAX302/M and DRV001, Thor Labs; 0.5-μm-bidirectional repeatability). A large glass dish was used to contain the distilled water; inside it sat the device, the EC probe, and a magnetic stir bar as shown in Figure 5.12(a). Attached to the stage was a shaft with double-sided adhesive tape at the protruding end (the tape ensures that retracting the shaft would

expand the chamber). The shaft was aligned to the center of the pump chamber as shown in Figure 5.12(b) and lowered until the chamber was completely compressed. Pump chambers with the different valve designs were actuated using this stage and all of them were visually found to work but only design (a) from Figure 3.5 was used for further testing.

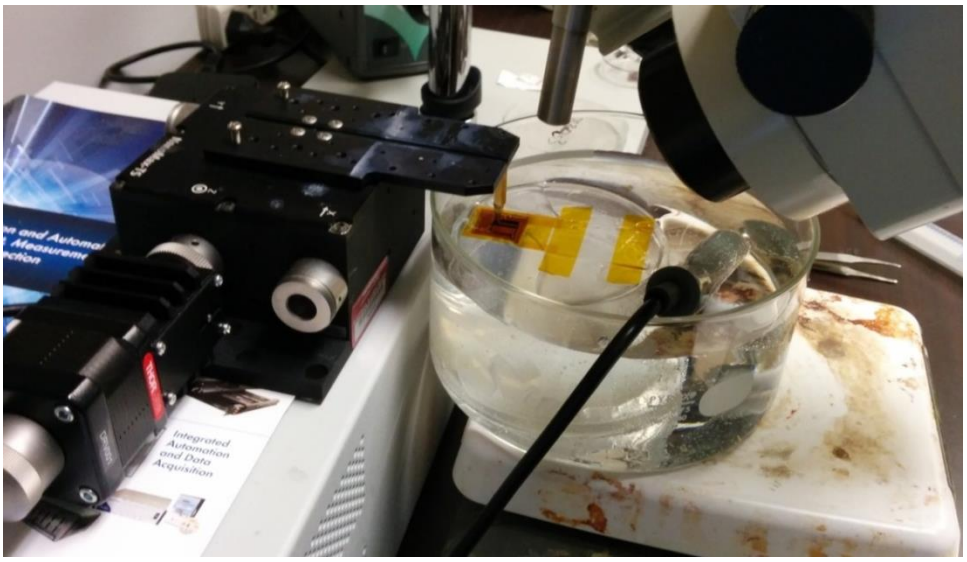

(a)

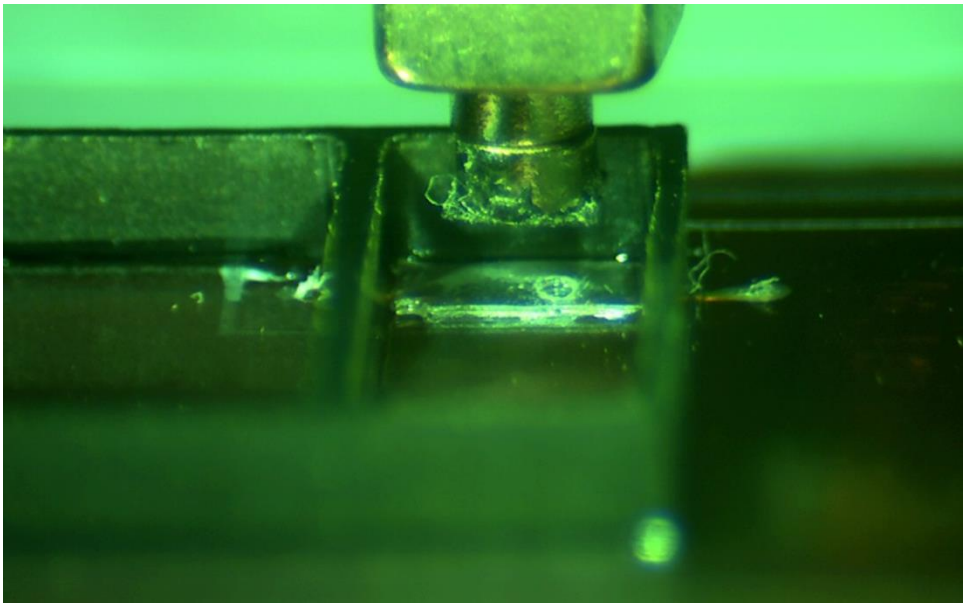

(b)

Figure 5.12: (a) Pumping the device using the 3-axis stage and (b) a close-up view of the shaft aligned with the Parylene pump chamber

The external stage was set to apply consecutive 250 μm displacements because it was close to the maximum stroke that the pump's diaphragm could safely make without the shaft separating from the pump chamber. The pump was repeatedly actuated 5 times every 3 min for a total of 5 sets, to vary the conductivity of the water medium with the ejected saline (3 min intervals were selected to reach stable conductivity of the medium). The conductivity of varying concentrations of NaCl [71] were interpolated to give the equation

$$G = 21304\mathrm{C} + 0.0904 \tag{5.1}$$

where $G$ is the conductivity in μS/cm and $C$ is the concentration in %. This equation shows an excellent fit with the reported data (within 0.95% error for the conductivity range involved in the current study) and with it, the measured conductivities were translated into concentrations of NaCl. Then the volume of liquid pumped out per set was determined with the equation

$$V_s = \frac{(C_f - C_i)V_w}{C_{NaCl}} \tag{5.2}$$

where $C_f$ is the concentration after the conductivity reading stabilized, $C_i$ is the concentration before the pumping started, $V_w$ is the volume of the surrounding water, and $C_{NaCl}$ is the saline concentration in the reservoir. The volume ejected per set is shown in Figure 5.13. Afterwards, tests with 10, 15, and 20 pumps per set were also performed. The average volume of liquid expelled was determined to be 497 nL/pump when the pump chamber is actuated 250 μm. By doing analysis similar to the previous test, the volume per pump for each amplitude was determined and plotted in Figure 5.14; the saturation seen after 200 μm of displacement is due to the expansion limit of the chamber structure noted above.

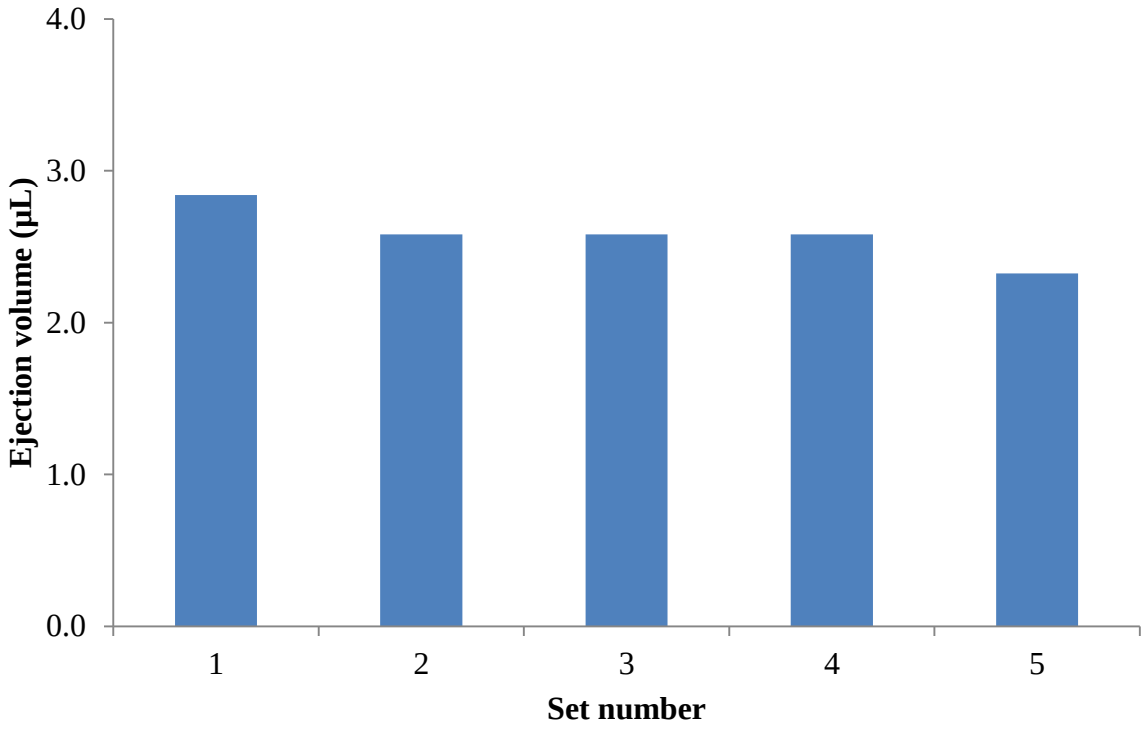


Figure 5.13: Ejection volume of 10% saline with five pumps per set

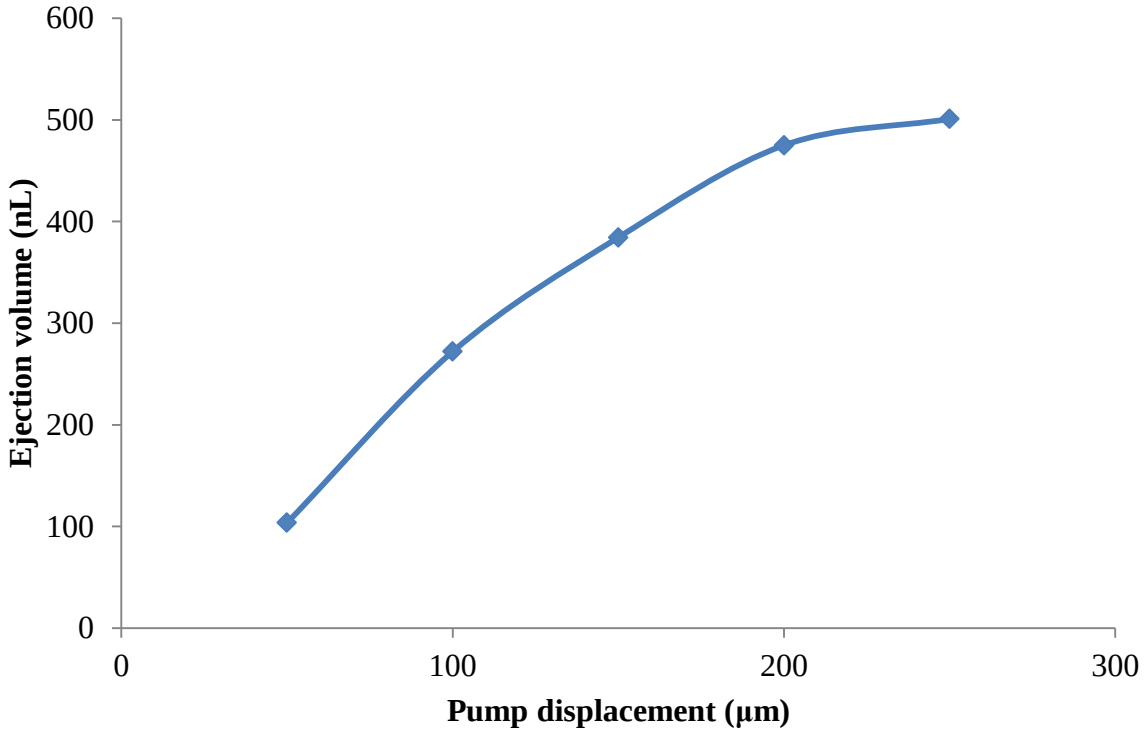


Figure 5.14: Dependence of ejection volume per actuation displacement for a single pump

### 5.3 Complete Device

After bonding the Nitinol actuator to the polyimide substrate but before bonding on the lid, the device was tested. Figure 5.15(a) shows the heating of the integrated actuator using an RF power of 0.85 W for 5 s. (This time period was selected to be the same as in the wireless release tests described later, which was revealed to be enough time to complete the release of a single pump, after which the actuator cooled down during a much longer resting time before making the subsequent pump.) The temperature reading at spot-1 (77.1 °C) indicates that the center of the coil exceeded $T_a$ (= 65 °C) which is necessary to actuate the Nitinol-coil cantilever. Spots-2 and -3 show the temperatures of water in the reservoir and near the outlet nozzle, respectively, suggesting that even the outlet region adjacent to (~1.0 mm away from) the actuator was still close to room temperature.

Exterior heating is another important factor in terms of the device design and packaging. Any heating on the exterior surfaces should be within a level that does not cause thermal damage to tissue (below ~43 °C [72]). In light of this aspect, the temperature distribution on the polyimide casing of a fully packaged chip was monitored while exciting the chip wirelessly under the same conditions. Figure 5.15(b) shows an IR image of the chip's back side after a 5 second activation, showing that the maximum temperature over the entire surface was 42.3 °C (at spot-1). The location of this highest temperature is reasonable as it is where the actuator's anchor is located and thus should experience the greatest level of heat flux (since the pump chamber or an air gap is present between the other parts of the actuator and the casing). This temperature is around the safe-level threshold and may need to be lowered by optimizing the device packaging and/or by simply using a different Nitinol composition with lower phase transition temperatures. Since there was ~560 μm of polyimide (two 127-μm-thick substrate layers and a 305-μm-thick spacer serving as the actuator's anchor) between the actuator and the bottom surface, this measurement indicates that the temperature on the top wall of the pump chamber likely reached a level greater than 42 °C (only had a 305-μm-thick spacer between the pump chamber and the actuator). Further characterization is needed to determine the actual temperature inside the pump chamber, possibly via direct temperature probing of the interior liquid with a modified set-up (e.g., thermocouple probing).

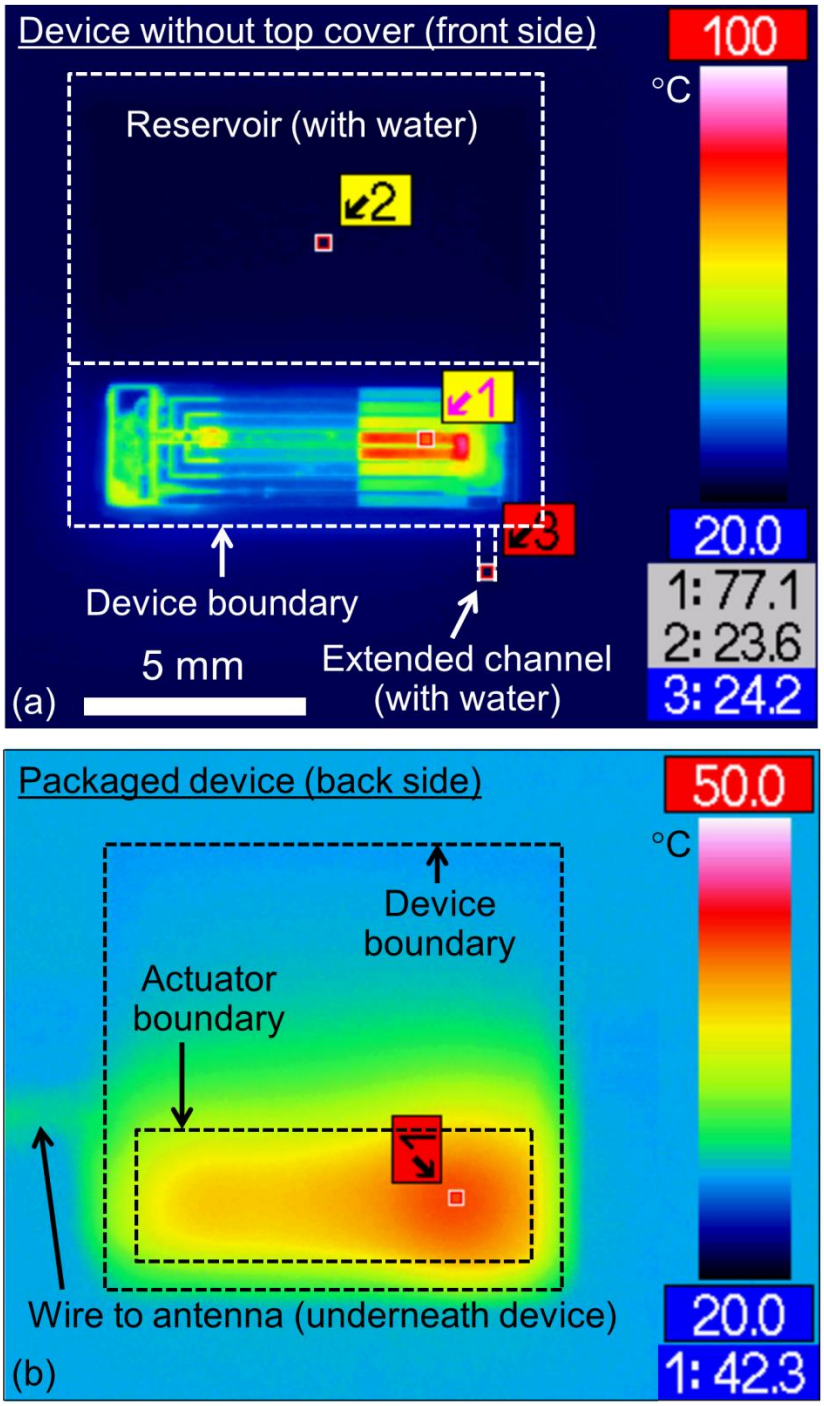


Figure 5.15: IR images of (a) the integrated actuator and the surrounding structures in an excited, open chip showing temperature readings of the actuator's innermost coil (spot-1), water in the reservoir (spot-2), and water at the outlet (spot-3); and (b) the fully packaged chip excited in the same manner showing the temperature distribution of the polyimide casing with a highest temperature of 42.3 °C appearing around the actuator's anchor region

Figure 5.16 shows the dynamic displacement response of the actuator/pump while wirelessly resonating the device for 5 s. The maximum displacement was substantially reduced compared to when the actuator was free, 83.5 µm versus 207 µm. This indicates that the actuator was able to partially compress the ~170-µm-thick chamber but did not produce enough force to fully squeeze it due to the reaction force produced by the water-filled pump chamber. Nevertheless, as discussed next in this section, the obtained displacement was found to be sufficient to achieve temporal ejections of solution from the device.

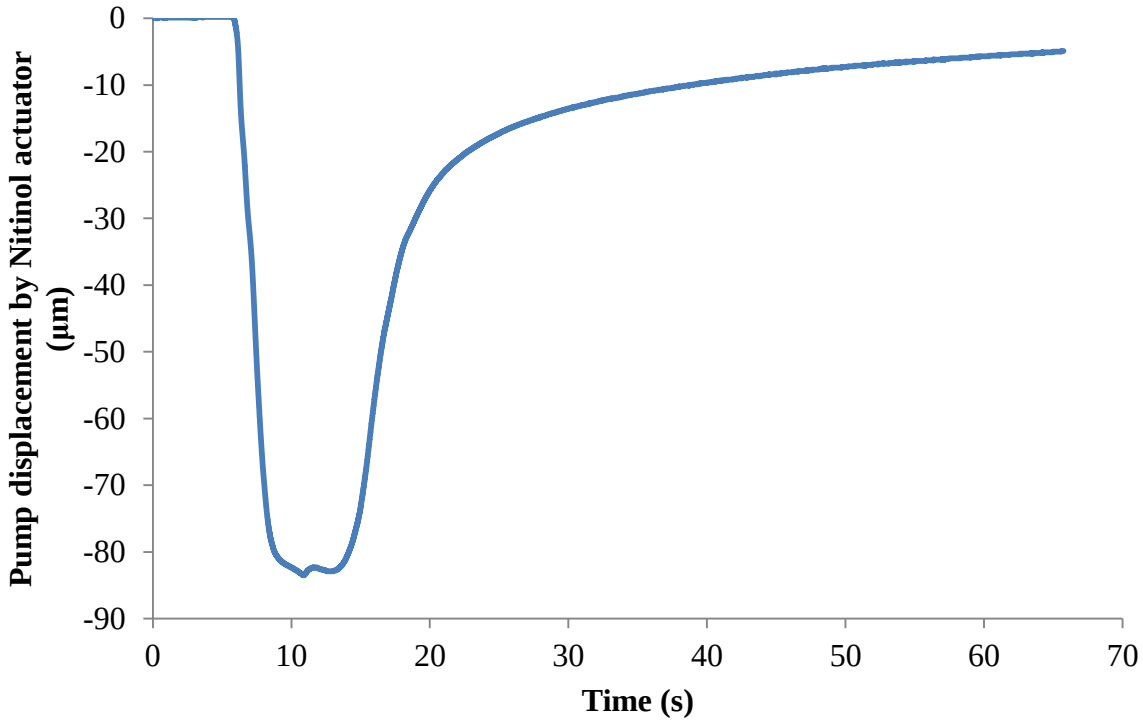


Figure 5.16: Displacement of a water-filled pump chamber produced by a wirelessly activated Nitinol actuator using an RF output power of 1.1 W

To determine the volume of liquid pumped out by the wirelessly activated device, tests measuring the conductivity change in the surrounding water were performed in a manner similar to the previous test, except 30-35% nitric acid was used to load the reservoir. Use of this highly conductive solution enabled the detection of a single pump through conductivity change (not available with the saline due to its lower conductance). Figure 5.17 shows the experimental set-up used for these tests.

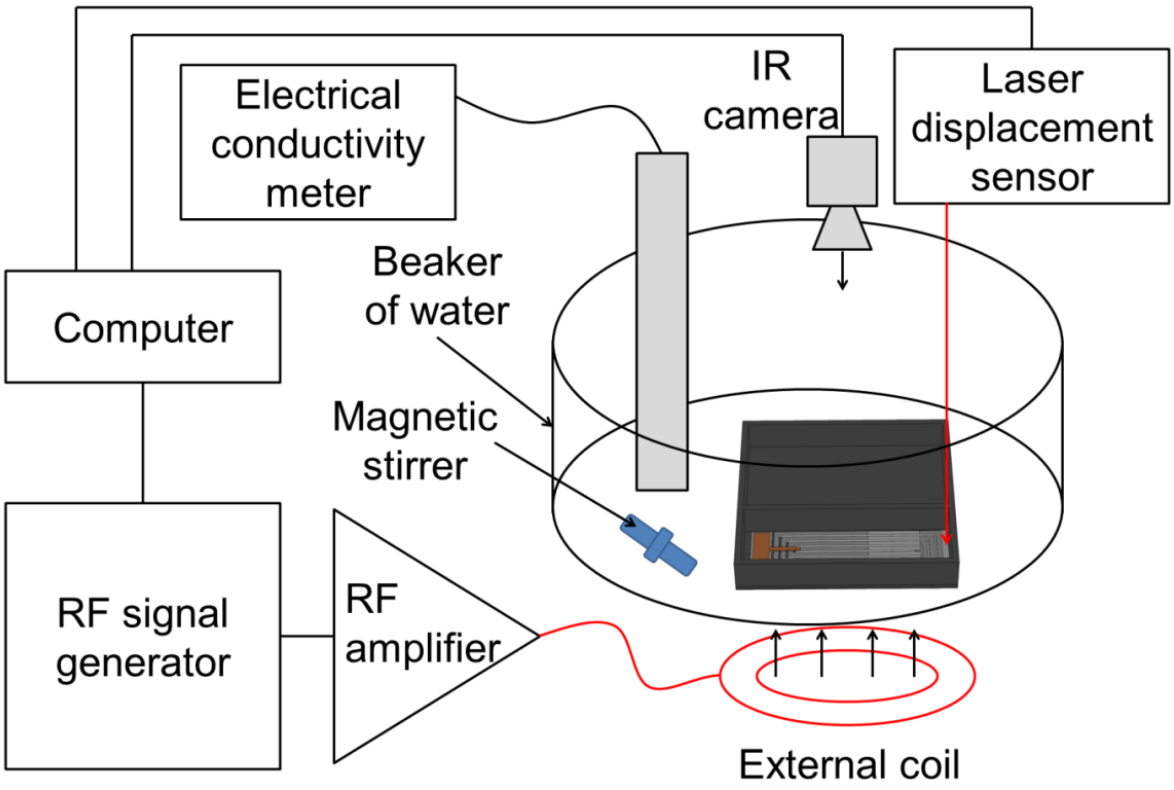


Figure 5.17: Experimental set-up for testing the performance of the complete device

The RF signal was turned on for 5 s and then the actuator was allowed to fully cool down for 85 s before it was heated again, allowing for uniform dispersion of the ejected agent and stabilization of the ambient conductivity. The position of the chip was adjusted to bring its outlet nozzle slightly above the water level but close enough to it so that a droplet coming out from the nozzle would be pulled away into the water. Figure 5.18 plots the cumulative amount of released agent (in moles, converted from the recorded conductivity data) as a function of time along with its temporal molar amount.

Interpolating the conductivity versus concentration data for $HNO_3$ [71] and using the same analysis as before, the average volume per pump from Figure 5.19 (except the first activation, which may have been affected by the initial priming of the pump and outlet channel) was determined to be 219 nL. Using the volume per pump versus actuation displacement plot in Figure 5.14 and the maximum displacement of 83.5 μm found in Figure 5.16, the pumping volume was interpolated to be 217 nL, agreeing well with the result of 219 nL.

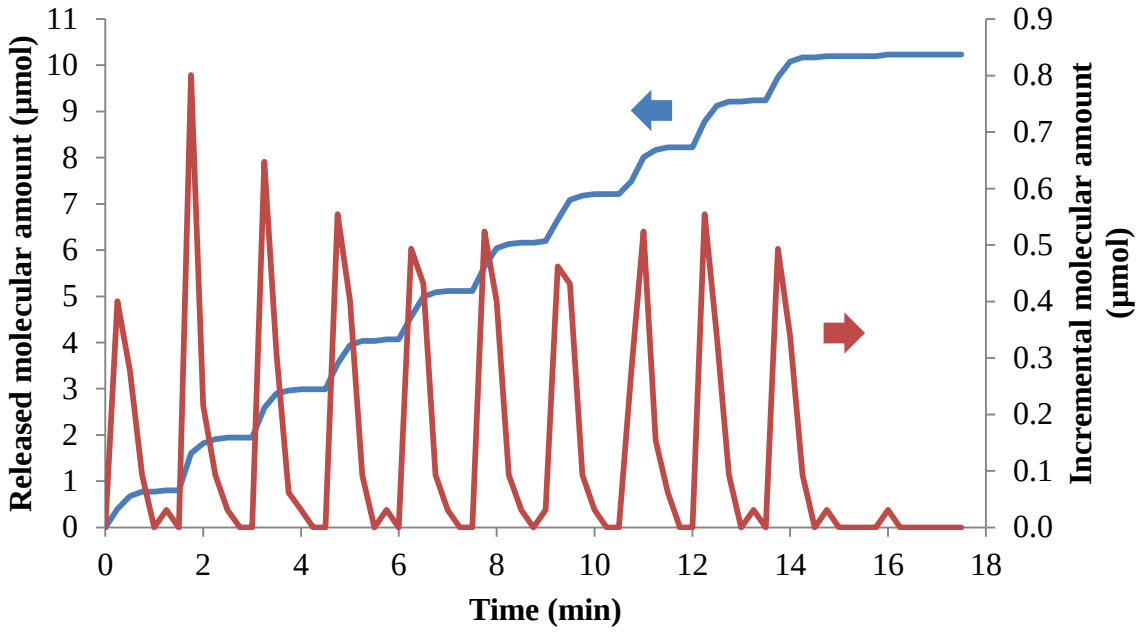


Figure 5.18: Cumulative and incremental molar amounts of released $HNO_3$ per pump quantified from the recorded conductivity change of the surrounding water by repeated ejections from the RF-excited DDD chip without submerging its outlet nozzle

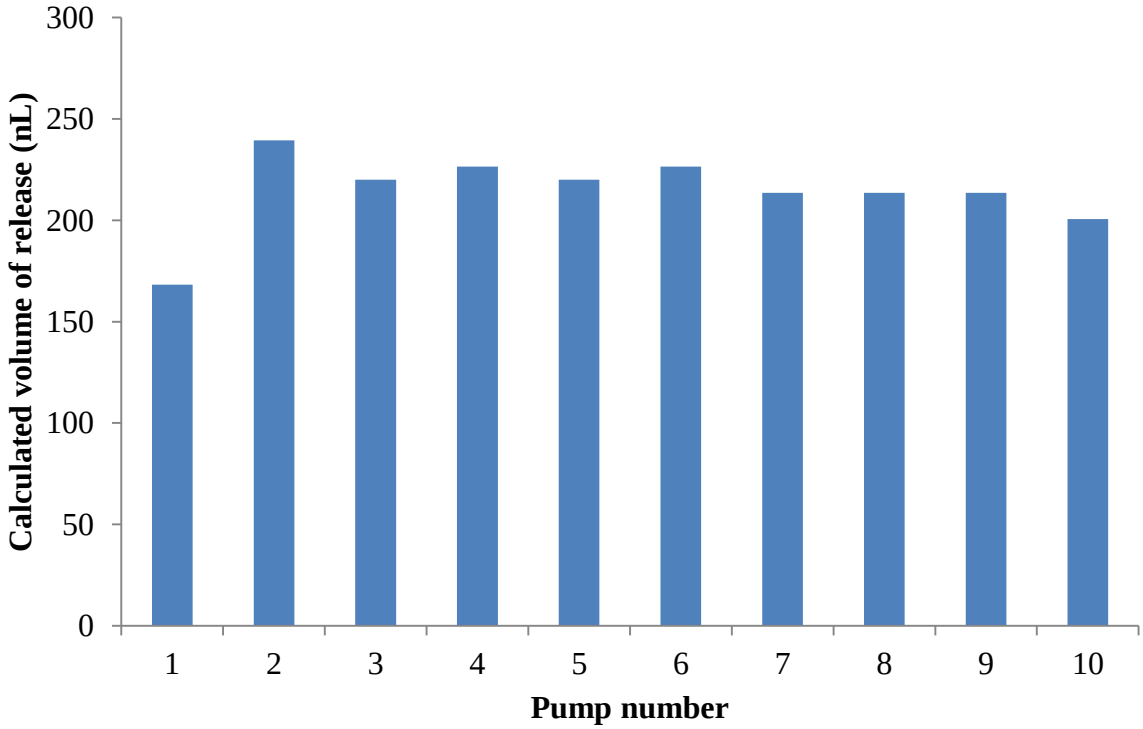


Figure 5.19: Released volume per pump of the DDD without submerging its outlet nozzle

A single ejection of 219 nL along with a reservoir capacity of 76 μL (measured later in this section), suggests that the chip can be pumped ~350 times before requiring a refill. As an example of its clinical relevance, human parathyroid hormone fragment (1-34) (hPTH(1-34)) is used for anabolic treatment of osteoporosis and is shown to reduce the occurrence of bone fractures when drug doses of 20-40 μg are administered daily [73], [74]. With 40 μg daily doses and a solubility of 80 mg/mL [20], the developed DDD could be used for 5 months before refilling; in comparison with the device from MicroCHIPS for this application [20], the above period is much longer than their capacity of 20 days and is provided by a DDD with a >80× smaller device volume. It should also be noted that the developed chip's capacity can be easily increased by simply enlarging the drug reservoir (e.g., doubling its height) while maintaining its miniaturized form with a lateral size of ~10 mm.

As a preliminary test of wireless pumping and release from a fully submerged device for visual verification, a fabricated chip's reservoir and pump chamber were filled/primed with a dye solution (food coloring). With a small syringe (100 μL, Hamilton), it was found that the reservoir had a capacity of 76 μL. The chip was immersed in distilled water (gently agitated with the magnetic stirrer) and excited with a tuned RF field radiated from the antenna located outside of the water-filled plastic container. The RF signal was repeatedly activated with a cycle of 5 seconds on and 13 seconds off. Ejection of the dye solution into the surrounding water was clearly observable as shown in Figure 5.20(a). With no agitation, cumulative release of the dye near the outlet nozzle was evident as shown in Figure 5.20(b).These tests qualitatively validated the device's functionality in a liquid ambient.

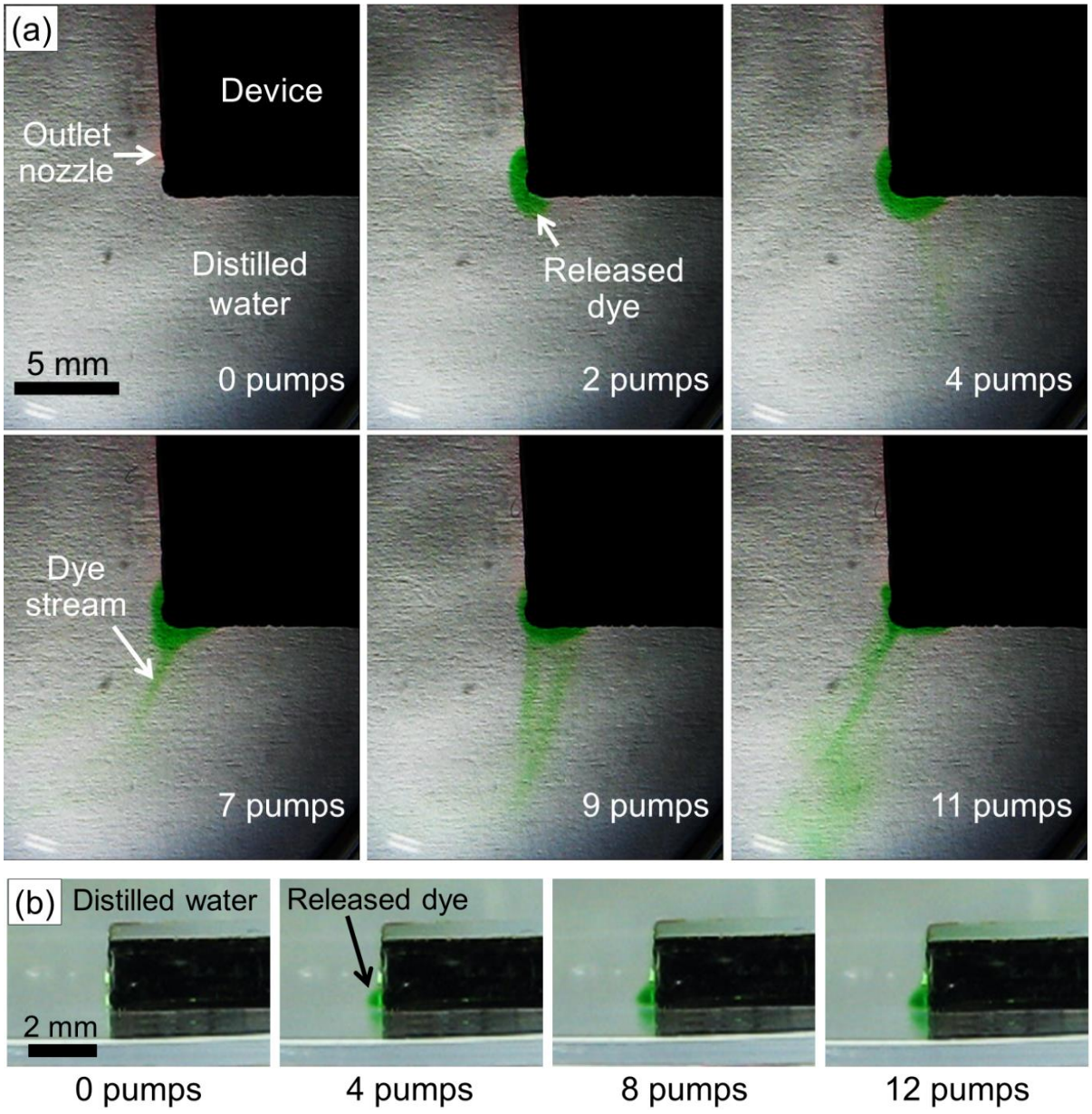


Figure 5.20: Images from the preliminary test of controlled wireless release through a fabricated DDD chip, with color dye, immersed in distilled water (a) with and (b) without flow. The chip was periodically excited by radiating an RF field (tuned to the $f_R$ of the device) with an output power of 1.1 W

The temporal release test was also conducted with a fully submerged device loaded with the $HNO_3$ solution and its pumping volume was evaluated by measuring the change in conductivity of the surrounding water. As shown in Figure 5.21, the device was pumped every 90 s for a total of 10 pumps.

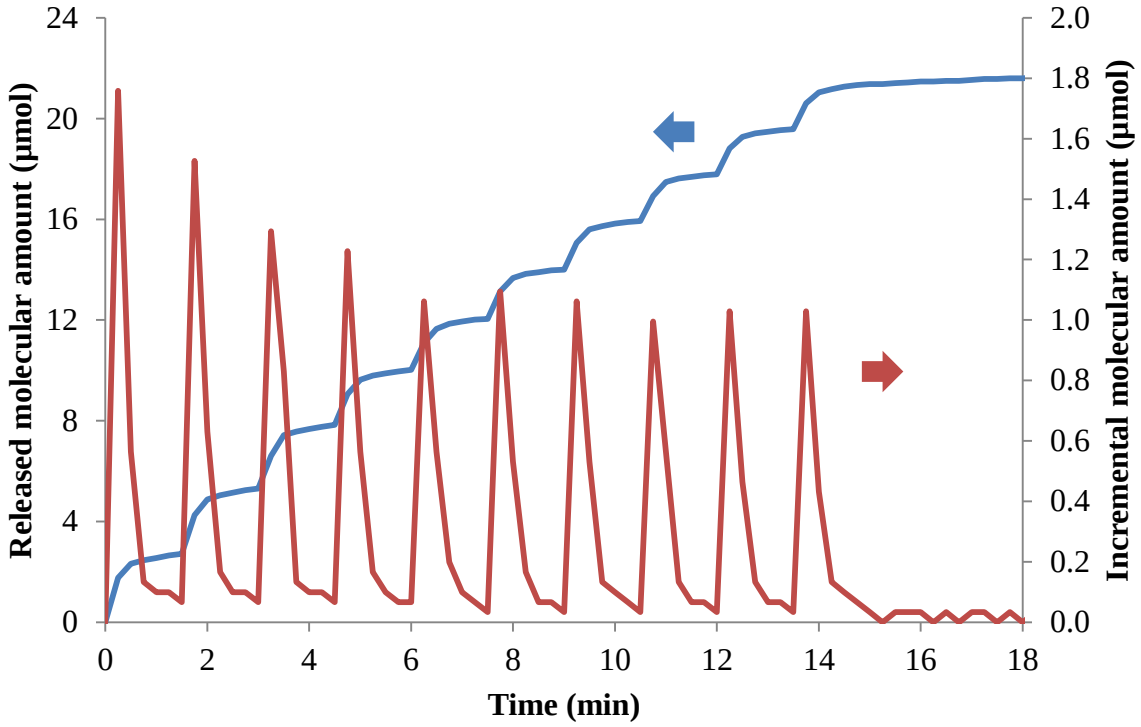


Figure 5.21: Cumulative and incremental molar amounts of released $HNO_3$ per pump quantified from the recorded conductivity change of the surrounding water by repeated ejections from the RF-excited DDD chip completely immersed in water

The volume ejected per pump was calculated (after accounting for the very small leakage observable in the conductivity data) and is plotted in blue in Figure 5.22. The volume released each pump shows an apparent tendency of gradual decrease followed by saturation with subsequent pumping. This outcome seems to be led by the condition that a small amount of water from the surroundings was drawn back into the pump chamber during operation, as suggested by Figure 5.21 that indicates a consistent decreasing trend in the ejected molar amount (or in the conductivity gain of the surroundings). When backflow is present, the concentration of the agent in the pump chamber is reduced, consequently affecting the

volume calculation. Knowing the molar change with each pump (quantified with the recorded conductivity data), the volume calculation can be compensated to estimate the actual volume of ejection. By comparing the molar amount of the agent ejected from one pump with the prior pump (Figure 5.21), the average decrease per pump was found to be ~5%. Then each pump's volume was corrected by a factor of $1.05^{(n-1)}$ where *n* is the pump number. The result (in red in Figure 5.22) suggests that the actual release volume is relatively constant around 400-450 nL/pump (larger than in Figure 5.19 as a different device with a taller pump chamber was used).

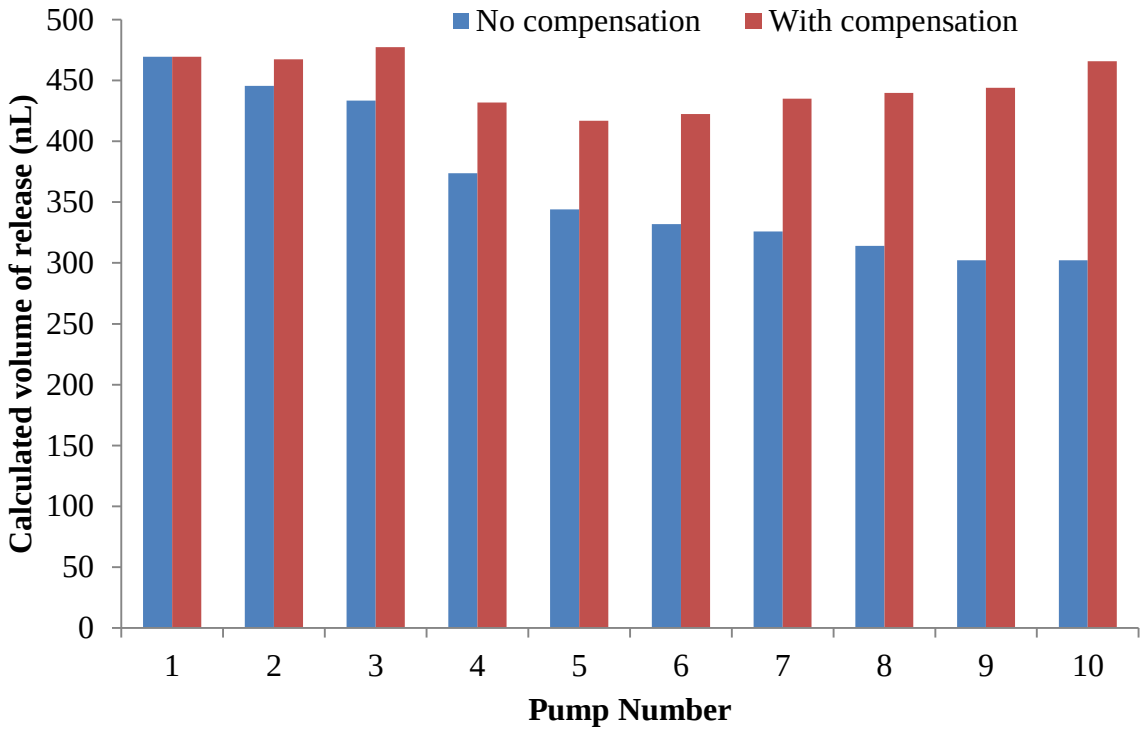


Figure 5.22: Released volume per pump of the completely immersed DDD with no backflow compensation in blue and with compensation in red to estimate the actual volume

A possible reason for this backflow is that the retracting (upward) force provided by the Nitinol actuator was not adequate to expand the pump chamber fast enough. (Note that the upward force is generated by the $SiO_2$ stress layer and not by the Nitinol that generates the downward force utilized to squeeze the pump; it is known that the force produced by the stress layer is smaller than the force produced by the Nitinol [60].) Because the check valves

are passive, a pressure difference is required to fully close them; if the pump chamber expands without providing the required pressure difference, the outlet valve may remain slightly open and allow for backflow. If this is the case, the test agent coming from the reservoir is mixed with the surrounding fluid coming through the outlet valve; thus the subsequent pump is diluted and the conductivity gain is lowered. This hypothesis is supported by the experimental result from Figure 5.19 that shows a relatively consistent pumping volume when the outlet is positioned right above the water level, hence physically preventing any backflow. Nevertheless, the experiment indeed demonstrates that ejections from the DDD can be radio-controlled with the developed prototype via resonant RF power transfer to the integrated Nitinol actuator.

As evident from Figure 5.22, the presence of backflow affects the precision of the delivered dose. To address this issue, the valves could use more compliant tethers (so that less pressure is required to fully close the valves) or use slanted tethers that apply a force on the disc against the seat to help the valve close [75]. Another potential method is to incorporate active valves; for example, thermoresponsive hydrogel valves [43] could be integrated and synchronously controlled with the actuator using the same RF excitation principle by assigning them wireless heaters with different resonant frequencies and by modulating the RF field corresponding to these frequencies [44]. This could offer not only complete valve closure but also full controllability over the valves.

# Chapter 6: Conclusion

In this thesis a wirelessly activated, implantable drug delivery device with an integrated SMA actuator was designed, fabricated, and tested. It was made from the biocompatible materials polyimide, Parylene-C, and nickel titanium alloy. The actuator was micromachined from Nitinol into a planar, rectangular spiral coil using μEDM. Compressive layers of $SiO_2$ on the Nitinol were micropatterned to adjust the profile of the inductive structure and its actuation range. Acting as a cantilever, the free end was displaced in martensite phase and was flat in austenite phase. A capacitor was monolithically integrated onto this Nitinol inductor to form a resonant *LC* circuit, serving as a frequency-selective wireless heater for out-of-plane actuation. The cantilever actuators were found to have a maximum actuation displacement of 215 μm and generate up to 71 mN of force. Heat generation, actuation displacement, and force generation were shown to be controllable by varying either the field frequency or the RF output power. The thermomechanical behaviors of the fabricated actuators were characterized to reveal a force generation >2× a previously reported Nitinol actuator (based on the same self-heating mechanism) with comparable RF power. Similar temporal response with 50% the applied power was found as well. The form factor of the developed actuator may be advantageous in increasing its usability and application range as cantilevers are widespread in MEMS designs. Exploiting the advantage, this wireless actuator could, with proper packaging, be applied to a variety of biomedical applications including micropumps and microvalves for implantable microfluidics, such as the developed DDD. Because the actuation can be controlled by the field frequency, an array of these actuators could be implemented into a single device while allowing control over individual actuators. This potentially not only enables complex tasks in a device but also contributes to its miniaturization as actuation control can be implemented in a fully passive manner without the need for separate control circuitry or an internal power source.

After the actuator and the pump chamber were independently tested, they were bonded together to form the entire drug delivery device. Wireless delivery was experimentally demonstrated using microfabricated prototypes in water. The prototypes were revealed to be able to release consistent volumes of the agents with controlled timings upon RF radiation.

The device was found to exhibit partial compression of the pump chamber and some backflow of the surrounding medium into the pump chamber during its expansion mode; possible causes of the phenomena and their solutions were proposed. The demonstrated delivery volume of 219 nL/pump and drug capacity of 76 μL suggest that the chip could be functional for up to 5 months without refilling in case of the application for anabolic osteoporosis treatment. The promising results obtained encourage further development.

There are several key aspects of this design that could be improved for greater and more consistent performance. In particular, backflow needs to be addressed by altering the design of the valves. Also, as shown when measuring the force generated by the actuator, a larger displacement of the free end resulted in a larger force; this could be achieved by using a thicker oxide layer or by patterning it differently. A larger force would compress the chamber further and expel more fluid per pump. Better heat distribution in the actuator would also affect the force since the outer turns were not fully in austenite phase. One possibility is to fill in the gaps between the coil turns with a thermally but not electrically conductive material (e.g. thermally conductive epoxy), promoting heat flux from the central region of the coil to its perimeters while preserving the inductive function of the Nitinol coil. Another improvement aspect was that manually applying the sacrificial photoresist to shape the pump chambers resulted in varying thicknesses between samples. Spin coating with a photoresist more suitable for producing very thick layers would significantly increase the consistency of the pumping volume across multiple devices. Lastly, the polyimide adhesive used to bond all the components together should be replaced with a biocompatible adhesive that does not require high temperature curing. In the prototypes, the polyimide adhesive was solidified but not fully cured at 300 °C because of the damage that would have occurred to the Parylene layers.

## Bibliography


[1] K. S. Pang, “Metabolic first-pass effects,” *J. Clin. Pharmacol.*, vol. 26, no. 8, pp. 580–582, 1986.

[2] N. Elman and U. Upadhyay, “Medical applications of implantable drug delivery microdevices based on MEMS (Micro-Electro-Mechanical-Systems),” *Curr. Pharm. Biotechnol.*, vol. 11, pp. 398–403, 2010.

[3] M. J. Cima, H. Lee, K. Daniel, L. M. Tanenbaum, A. Mantzavinou, K. C. Spencer, Q. Ong, J. C. Sy, J. Santini, C. M. Schoellhammer, D. Blankschtein, and R. S. Langer, “Single compartment drug delivery,” *J. Control. Release*, vol. 190, pp. 157–171, May 2014.

[4] L. Rasmussen and A. Arvin, “Chemotherapy-induced immunosuppression,” *Environ. Health Perspect.*, vol. 43, pp. 21–25, Feb. 1982.

[5] R. R. Love, H. Leventhal, D. V Easterling, and D. R. Nerenz, “Side effects and emotional distress during cancer chemotherapy,” *Cancer*, vol. 63, no. 3, pp. 604–612, Feb. 1989.

[6] M. Westphal and D. Hilt, “A phase 3 trial of local chemotherapy with biodegradable carmustine (BCNU) wafers (Gliadel wafers) in patients with primary malignant glioma,” *Neuro. Oncol.*, vol. 5, no. 2, pp. 79–88, 2003.

[7] D. L. Citrin, M. I. Resnick, P. Guinan, N. Al-Bussam, M. Scott, T. C. Gau, and G. T. Kennealey, “A comparison of Zoladex® and DES in the treatment of advanced prostate cancer: Results of a randomized, multicenter trial,” *Prostate*, vol. 18, no. 2, pp. 139–146, 1991.

[8] G. J. Jaffe, D. Martin, D. Callanan, P. A. Pearson, B. Levy, and T. Comstock, “Fluocinolone acetonide implant (Retisert) for noninfectious posterior uveitis: thirty-four-week results of a multicenter randomized clinical study,” *Ophthalmology*, vol. 113, no. 6, pp. 1020–1027, Jun. 2006.

[9] R. Shawgo and A. R. Grayson, “BioMEMS for drug delivery,” *Curr. Opin. Solid State Mater. Sci.*, vol. 6, pp. 329–334, 2002.

[10] G. Voskerician, M. S. Shive, R. S. Shawgo, H. Von Recum, J. M. Anderson, M. J. Cima, and R. Langer, “Biocompatibility and biofouling of MEMS drug delivery devices,” *Biomaterials*, vol. 24, no. 11, pp. 1959–1967, May 2003.

[11] N.-C. Tsai and C.-Y. Sue, “Review of MEMS-based drug delivery and dosing systems,” *Sensors Actuators A Phys.*, vol. 134, no. 2, pp. 555–564, Mar. 2007.

[12] N. M. Elman, H. L. Ho Duc, and M. J. Cima, “An implantable MEMS drug delivery device for rapid delivery in ambulatory emergency care,” *Biomed. Microdevices*, vol. 11, no. 3, pp. 625–631, Jun. 2009.

[13] J. M. Maloney, S. a Uhland, B. F. Polito, N. F. Sheppard, C. M. Pelta, and J. T. Santini, “Electrothermally activated microchips for implantable drug delivery and biosensing,” *J. Control. Release*, vol. 109, no. 1–3, pp. 244–255, Dec. 2005.

[14] J. H. Prescott, S. Lipka, S. Baldwin, N. F. Sheppard, J. M. Maloney, J. Coppeta, B. Yomtov, M. a Staples, and J. T. Santini, “Chronic, programmed polypeptide delivery from an implanted, multireservoir microchip device,” *Nat. Biotechnol.*, vol. 24, no. 4, pp. 437–438, Apr. 2006.

[15] Y. Yang, Y. Huang, and H. Liao, “A release-on-demand wireless CMOS drug delivery SoC based on electrothermal activation technique,” in *Solid-State Circuits Conference*, 2009, pp. 288–290.

[16] J. Santini, M. Cima, and R. Langer, “A controlled-release microchip,” *Nature*, vol. 397, no. 17, pp. 335–338, 1999.

[17] Y. Li, R. S. Shawgo, B. Tyler, P. T. Henderson, J. S. Vogel, A. Rosenberg, P. B. Storm, R. Langer, H. Brem, and M. J. Cima, “In vivo release from a drug delivery MEMS device,” *J. Control. Release*, vol. 100, no. 2, pp. 211–9, Nov. 2004.

[18] R. S. Shawgo, G. Voskerician, H. L. H. Duc, Y. Li, A. Lynn, M. MacEwan, R. Langer, J. M. Anderson, and M. J. Cima, “Repeated in vivo electrochemical activation and the biological effects of microelectromechanical systems drug delivery device,” *J. Biomed. Mater. Res. A*, vol. 71, no. 4, pp. 559–68, Dec. 2004.

[19] “Microchips web page.” [Online]. Available: http://www.mchips.com/index.html. [Accessed: 31-Jul-2014].

[20] R. Farra, N. F. Sheppard, L. McCabe, R. M. Neer, J. M. Anderson, J. T. Santini, M. J. Cima, and R. Langer, “First-in-human testing of a wirelessly controlled drug delivery microchip,” *Sci. Transl. Med.*, vol. 4, no. 122, p. 122ra21, Feb. 2012.

[21] A. Nisar, N. Afzulpurkar, B. Mahaisavariya, and A. Tuantranont, “MEMS-based micropumps in drug delivery and biomedical applications,” *Sensors Actuators B Chem.*, vol. 130, no. 2, pp. 917–942, Mar. 2008.

[22] O. Smal, B. Dehez, B. Raucent, M. De Volder, J. Peirs, D. Reynaerts, F. Ceyssens, J. Coosemans, and R. Puers, “Modelling, characterization and testing of an ortho-planar micro-valve,” *J. Micro-Nano Mechatronics*, vol. 4, no. 3, pp. 131–143, Nov. 2008.

[23] P. Chen and D. Rodger, “Floating-disk parylene microvalves for self-pressure-regulating flow controls,” *J. Microelectromechanical Syst.*, vol. 17, no. 6, pp. 1352–1361, 2008.

[24] W. L. Benard, H. Kahn, A. H. Heuer, and M. A. Huff, “Thin-film shape-memory alloy actuated micropumps,” *J. Microelectromechanical Syst.*, vol. 7, no. 2, pp. 245–251, Jun. 1998.

[25] P. Galambos and J. Lantz, “Active MEMS valves for flow control in a high-pressure micro-gas-analyzer,” *J. Microelectromechanical Syst.*, vol. 20, no. 5, pp. 1150–1162, 2011.

[26] R. Lo, P.-Y. Li, S. Saati, R. N. Agrawal, M. S. Humayun, and E. Meng, “A passive MEMS drug delivery pump for treatment of ocular diseases,” *Biomed. Microdevices*, vol. 11, no. 5, pp. 959–970, Oct. 2009.

[27] A. Machauf, Y. Nemirovsky, and U. Dinnar, “A membrane micropump electrostatically actuated across the working fluid,” *J. Micromechanics Microengineering*, vol. 15, no. 12, pp. 2309–2316, Dec. 2005.

[28] A. Doll, M. Heinrichs, F. Goldschmidtboeing, H.-J. Schrag, U. T. Hopt, and P. Woias, “A high performance bidirectional micropump for a novel artificial sphincter system,” *Sensors Actuators A Phys.*, vol. 130–131, pp. 445–453, Aug. 2006.

[29] T. Pan, S. J. McDonald, E. M. Kai, and B. Ziaie, “A magnetically driven PDMS micropump with ball check-valves,” *J. Micromechanics Microengineering*, vol. 15, no. 5, pp. 1021–1026, May 2005.

[30] Y. Yang, Z. Zhou, X. Ye, and X. Jiang, “Bimetallic thermally actuated micropump,” *Am. Soc. Mech. Eng. Dyn. Syst. Control Div.*, vol. 59, pp. 351–354, 1996.

[31] R. Sheybani, H. Gensler, and E. Meng, “A MEMS electrochemical bellows actuator for fluid metering applications,” *Biomed. Microdevices*, vol. 15, no. 1, pp. 37–48, Feb. 2013.

[32] J. Barth, C. Megnin, and M. Kohl, “A Bistable Shape Memory Alloy Microvalve With Magnetostatic Latches,” *J. Microelectromechanical Syst.*, vol. 21, no. 1, pp. 76–84, Feb. 2012.

[33] D. J. Bell, T. J. Lu, N. A. Fleck, and S. M. Spearing, “MEMS actuators and sensors: observations on their performance and selection for purpose,” *J. Micromechanics Microengineering*, vol. 15, no. 7, pp. S153–S164, Jul. 2005.

[34] A. C. Tikka, “Loading analysis of a remotely interrogatable passive microvalve,” in *Recent Advances in Sensing Technology*, Berlin: Springer, Heidelberg, 2009, pp. 169–188.

[35] P. Basset, A. Kaiser, B. Legrand, D. Collard, and L. Buchaillot, “Complete System for Wireless Powering and Remote Control of Electrostatic Actuators by Inductive Coupling,” *IEEE/ASME Trans. Mechatronics*, vol. 12, no. 1, pp. 23–31, Feb. 2007.

[36] M. Khoo and C. Liu, “Micro magnetic silicone elastomer membrane actuator,” *Sensors Actuators A Phys.*, vol. 89, no. 3, pp. 259–266, Apr. 2001.

[37] M. Sendoh, K. Ishiyama, and K. I. Arai, “Fabrication of magnetic actuator for use in a capsule endoscope,” *IEEE Trans. Magn.*, vol. 39, no. 5, pp. 3232–3234, Sep. 2003.

[38] C. Liu, D. Zhang, and H. Zhang, “Experimental study of novel microactuator based on photothermal expansion,” *Optoelectron. Lett.*, vol. 4, no. 2, pp. 89–91, Apr. 2008.

[39] S. S. Zaidi, F. Lamarque, J. Favergeon, O. Carton, C. Prelle, M. Lejeune, and A. Zeinert, “Wavelength Dependent Remote Power Supply for Shape Memory Alloy,” *J. Intell. Mater. Syst. Struct.*, vol. 21, no. 2, pp. 175–184, Nov. 2009.

[40] M. S. Mohamed Ali and K. Takahata, “Frequency-controlled wireless shape-memory-alloy microactuators integrated using an electroplating bonding process,” *Sensors Actuators A Phys.*, vol. 163, no. 1, pp. 363–372, Sep. 2010.

[41] P.-Y. Li, J. Shih, R. Lo, S. Saati, R. Agrawal, M. S. Humayun, Y.-C. Tai, and E. Meng, “An electrochemical intraocular drug delivery device,” *Sensors Actuators A Phys.*, vol. 143, no. 1, pp. 41–48, May 2008.

[42] H. Gensler, R. Sheybani, P.-Y. Li, R. Lo Mann, and E. Meng, “An implantable MEMS micropump system for drug delivery in small animals,” *Biomed. Microdevices*, vol. 14, no. 3, pp. 483–96, Jun. 2012.

[43] S. Rahimi, E. H. Sarraf, G. K. Wong, and K. Takahata, “Implantable drug delivery device using frequency-controlled wireless hydrogel microvalves,” *Biomed. Microdevices*, vol. 13, no. 2, pp. 267–277, Apr. 2011.

[44] M. S. Mohamed Ali and K. Takahata, “Wireless microfluidic control with integrated shape-memory-alloy actuators operated by field frequency modulation,” *J. Micromechanics Microengineering*, vol. 21, no. 7, p. 075005, Jul. 2011.

[45] H. Kahn, M. A. Huff, and A. H. Heuer, “The TiNi shape-memory alloy and its applications for MEMS,” *J. Micromechanics Microengineering*, vol. 8, no. 3, pp. 213–221, Sep. 1998.

[46] N. B. Morgan, “Medical shape memory alloy applications—the market and its products,” *Mater. Sci. Eng. A*, vol. 378, no. 1–2, pp. 16–23, Jul. 2004.

[47] N. Frantz, E. Dufour-Gergam, J. P. Grandchamp, a. Bosseboeuf, W. Seiler, G. Nouet, and G. Catillon, “Shape memory thin films with transition above room temperature from Ni-rich NiTi films,” *Sensors Actuators A Phys.*, vol. 99, no. 1–2, pp. 59–63, Apr. 2002.

[48] G. Rondelli, “Corrosion resistance tests on NiTi shape memory alloy,” *Biomaterials*, vol. 17, no. 20, pp. 2003–8, Oct. 1996.

[49] T. Duerig, A. Pelton, and D. Stöckel, “An overview of nitinol medical applications,” *Mater. Sci. Eng. A*, vol. 273–275, pp. 149–160, 1999.

[50] D. Stoeckel, “Nitinol medical devices and implants,” *Minim. Invasive Ther. Allied Technol.*, vol. 9, no. 2, pp. 81–88, Jan. 2000.

[51] A. R. Pelton, T. W. Duerig, and D. Stöckel, “A guide to shape memory and superelasticity in Nitinol medical devices,” *Minim. Invasive Ther. Allied Technol.*, vol. 13, no. 4, pp. 218–221, Aug. 2004.

[52] D. J. Wever, A. G. Veldhuizen, M. M. Sanders, J. M. Schakenraad, and J. R. van Horn, “Cytotoxic, allergic and genotoxic activity of a nickel-titanium alloy,” *Biomaterials*, vol. 18, no. 16, pp. 1115–1120, Aug. 1997.

[53] A. R. Pelton, D. Stöckel, and T. W. Duerig, “Medical Uses of Nitinol,” *Mater. Sci. Forum*, vol. 327–328, pp. 63–70, 2000.

[54] S. H. Mahdavi and P. J. Bentley, “Evolving Motion of Robots with Muscles,” *Appl. Evol. Comput.*, vol. 2611, pp. 651–660, 2003.

[55] K. K. Şafak and G. G. Adams, “Modeling and simulation of an artificial muscle and its application to biomimetic robot posture control,” *Rob. Auton. Syst.*, vol. 41, no. 4, pp. 225–243, 2002.

[56] M. Bergamasco, P. Dario, and F. Salsedo, “Shape memory alloy microactuators,” *Sensors Actuators A Phys.*, vol. 23, pp. 253–257, 1990.

[57] K. Mackenzie and D. Johnson, “Stress control of Si-based PECVD dielectrics,” in *Symp. Silicon Nitride and Silicon Dioxide Thin Insulating Films & Other Emerging Dielectrics VIII*, 2005, no. May, pp. 148–159.

[58] S. M. Sze and K. K. Ng, *Physics of Semiconductor Devices*, 3rd ed. Wiley, 2006.

[59] "Memry Co. web page." [Online]. Available: http://memry.com/nitinol-iq/nitinol-fundamentals/physical-properties. [Accessed: 08-Oct-2014].

[60] M. Ali, B. Bycraft, A. Bsoul, and K. Takahata, "Radio-Controlled Microactuator Based on Shape-Memory-Alloy Spiral-Coil Inductor," *J. Microelectromechanical Syst.*, vol. 22, no. 2, pp. 331–338, 2013.

[61] E. F. Hasselbrink, T. J. Shepodd, and J. E. Rehm, "High-pressure microfluidic control in lab-on-a-chip devices using mobile polymer monoliths," *Anal. Chem.*, vol. 74, no. 19, pp. 4913–8, Oct. 2002.

[62] J. Kim, J. Baek, K. Lee, Y. Park, K. Sun, T. Lee, and S. Lee, "Photopolymerized check valve and its integration into a pneumatic pumping system for biocompatible sample delivery," *Lab Chip*, vol. 6, no. 8, pp. 1091–4, Aug. 2006.

[63] B. Yang and Q. Lin, "Planar micro-check valves exploiting large polymer compliance," *Sensors Actuators A Phys.*, vol. 134, no. 1, pp. 186–193, Feb. 2007.

[64] X. Wang, Q. Lin, and Y. Tai, "A parylene micro check valve," in *Twelfth IEEE International Conference on Micro Electro Mechanical Systems*, 1999.

[65] P. Chen and D. Rodger, "Surface-micromachined parylene dual valves for on-chip unpowered microflow regulation," *J. Microelectromechanical Syst.*, vol. 16, no. 2, pp. 223–231, 2007.

[66] "Nitinol Technical Properties." [Online]. Available: http://jmmedical.com/resources/221/Nitinol-Technical-Properties.html. [Accessed: 31-Jul-2014].

[67] HD MicroSystems, "HD-3007 Adhesive Process Guide," 2010.

[68] V. Sridhar and K. Takahata, "A hydrogel-based passive wireless sensor using a flex-circuit inductive transducer," *Sensors Actuators A Phys.*, vol. 155, no. 1, pp. 58–65, Oct. 2009.

[69] S. Zinn and S. L. Semiatin, "Coil design and fabrication: basic design and modifications," in *Proceedings, Heat Treating*, 1988, no. June, pp. 32–36.

[70] R. P. Madding, "Emissivity measurement and temperature correction accuracy considerations," in *Proceedings, SPIE 3700, Thermosense XXI*, 1999, vol. 3700, pp. 393–401.

[71] Invensys Foxboro, "Conductivity Ordering Guide," 1999. [Online]. Available: http://myweb.wit.edu/sandinic/Research/conductivity v concentration.pdf. [Accessed: 23-Jul-2014].

[72] P. S. Yarmolenko, E. J. Moon, C. Landon, A. Manzoor, D. W. Hochman, B. L. Viglianti, and M. W. Dewhirst, "Thresholds for thermal damage to normal tissues: an update," *Int. J. Hyperthermia*, vol. 27, no. 4, pp. 320–343, Jan. 2011.

[73] R. M. Neer, C. D. Arnaud, J. R. Zanchetta, R. Prince, G. A. Gaich, J.-Y. Reginster, A. B. Hodsman, E. F. Eriksen, S. Ish-Shalom, H. K. Genant, O. Wang, and B. H. Mitlak, "Effect of parathyroid hormone (1-34) on fractures and bone mineral density in postmenopausal women with osteoporosis," *Obstet. Gynecol. Surv.*, vol. 56, no. 10, pp. 623–624, 2001.

[74] C. P. Jerome, D. B. Burr, T. Van Bibber, J. M. Hock, and R. Brommage, "Treatment with human parathyroid hormone (1-34) for 18 months increases cancellous bone volume and improves trabecular architecture in ovariectomized cynomolgus monkeys (Macaca fascicularis)," *Bone*, vol. 28, no. 2, pp. 150–159, Feb. 2001.

[75] J. C.-H. Lin, F. Yu, and Y.-C. Tai, "Cracking pressure control of parylene checkvalve using slanted tensile tethers," *2010 IEEE 23rd Int. Conf. Micro Electro Mech. Syst.*, vol. 2, no. 1, pp. 1107–1110, Jan. 2010.

# Appendix A: Detailed Parameters Used for Device Fabrication

**PECVD**

| Process | Power (W) | Pressure (mTorr) | Temperature (°C) | Gas flow (sccm) |
|---|---|---|---|---|
| Descum and $O_2$ plasma etch | 200 | 400 | 20 | $O_2$ = 80 |
| $SiO_2$ deposition | 200 | 500 | 300 | $N_2O$ = 64<br>DES = 4 |

**Photolithography**

| Photoresist | SPR220-7.0 | SPR220-7.0 | S1813 | PM240 |
|---|---|---|---|---|
| **Thickness** | 7 μm | ~170 μm (with iterative process) | 1.5 μm | 37 μm |
| **Spin coat** | 500 rpm and 220 rpm/s for 15 s<br>4000 rpm and 2090 rpm/s for 30 s | N/A (manual application) | 500 rpm and 220 rpm/s for 15 s<br>4000 rpm and 2090 rpm/s for 60 s | N/A, laminated on at 1.5 feet per minute and 105 °C |
| **Soft bake** | 115 °C for 2 min | 75 °C for 3 h | 115 °C for 1 min | N/A |
| **Exposure** | 12 min<br>(MJB-3) | 3x 3:20 min<br>(Canon) | 6 min<br>(MJB-3) | 5:30 min<br>(MJB-3) |
| **Rehydrate** | 1 h | 1 h | N/A | N/A |
| **Post exposure bake** | 115 °C for 2 min | N/A | N/A | N/A |
| **Development** | MF-24A for 1:45 min | MF-24A for 15 min | MF319 for 1:30 min | 1% $NaCO_3$ for 4 min |
| **Stripper** | Acetone | Acetone | Acetone | 3% KOH |

**Polyimide Dielectric Layer (2.64 µm)**

Spin coat at 1000 rpm and 550 rpm/s for 10 s followed by 3000 rpm and 1540 rpm/s for 60 s. Soft bake at 90 °C for 90 s followed by 120 °C for another 90 s. Then load the sample into the PECVD and set the temperature to 200 °C. Hold it at 200 °C for 30 min then increase the temperature to 300 °C. After holding it at 300 °C for 1 h, cool it back down to room temperature. The pressure is set to 1000 mTorr with 15 sccm of $N_2$ during heating and 50 sccm of $N_2$ during cooling.